Check for updates

JGR Space Physics

RESEARCH ARTICLE
10.1029/2025JA034738

Comprehensive Characterization of Water Group Ion Composition and Distributions in Saturn's Magnetosphere With Cassini Plasma Spectrometer Data

Thomas K. Kim[1], D. B. Reisenfeld[1], R. J. Wilson[2], H. T. Smith[3], A. K. Woodson[4], F. Allegrini[5,6], R. W. Ebert[5,6], M. G. Henderson[1], P. K. Kollmann[3], G. Livadiotis[7], G. Nicolaou[8], J. R. Szalay[7], P. W. Valek[5], and A. Masters[9]

[1]Los Alamos National Laboratory, Space Science and Applications Group (ISR-1), Los Alamos, NM, USA, [2]Laboratory for Atmospheric and Space Physics, Boulder, CO, USA, [3]The Johns Hopkins University Applied Physics Laboratory, Laurel, MD, USA, [4]The University of Virginia, Charlottesville, VA, USA, [5]Space Science and Engineering Division, Southwest Research Institute, San Antonio, TX, USA, [6]Department of Physics and Astronomy, University of Texas at San Antonio, San Antonio, TX, USA, [7]Department of Astrophysical Sciences, Princeton University, Princeton, NJ, USA, [8]Mullard Space Science Laboratory, University College London, London, UK, [9]Department of Physics, Imperial College London, London, UK

Key Points:

- Enceladus-origin OH^+, H_2O^+, and H_3O^+ dissociate within 5–10 Saturn radii, leaving O^+ and H^+ dominant
- Ionosphere-plasma coupling is strongest at 5–10 Saturn radii, where flow speeds reach about 80% of rigid corotation
- O^+ ions make up nearly 70% of Saturn's thermal plasma population across the magnetosphere out to 16 Saturn radii

Correspondence to:
T. K. Kim,
thomaskim@lanl.gov

Citation:
Kim, T. K., Reisenfeld, D. B., Wilson, R. J., Smith, H. T., Woodson, A. K., Allegrini, F., et al. (2026). Comprehensive characterization of water group ion composition and distributions in Saturn's magnetosphere with Cassini plasma spectrometer data. *Journal of Geophysical Research: Space Physics*, *131*, e2025JA034738. https://doi.org/10.1029/2025JA034738

Received 7 OCT 2025
Accepted 18 MAR 2026
Corrected 15 APR 2026

This article was corrected on 15 APR 2026. See the end of the full text for details.

Abstract Saturn's magnetosphere is continuously supplied with neutrals from the Enceladus plume and the icy rings, which undergo ionization and charge-exchange to form a complex water-group plasma environment. While the Cassini Plasma Spectrometer (CAPS) instrument has provided extensive compositional information, detailed separation of individual water-group ion species in time-of-flight (TOF) data has not previously been achieved. In this study, we perform forward modeling of CAPS-IMS energy-per-charge (E/Q) and TOF spectra obtained between 2004 and 2012 to resolve O^+, OH^+, H_2O^+, and H_3O^+ and to characterize their plasma properties, including number density, temperature, and thermodynamic κ. Our results demonstrate that O^+ is the dominant thermal ion species throughout Saturn's magnetosphere, comprising up to ∼70% of the total ion population beyond ∼5 Saturn radii (R_S). In contrast, molecular ions such as OH^+, H_2O^+, and H_3O^+ dominate closer to Enceladus but rapidly dissociate into atomic ions between ∼5 and 10 R_S. This radial region is also characterized by the steepest increase in plasma flow speed, which rises from ∼40% to ∼80% of rigid corotation. Simultaneously, ion velocity distributions approach Maxwell–Boltzmann equilibrium, as indicated by high kappa values. These findings provide new constraints on the ion–neutral chemistry that regulates the balance between molecular and atomic ions in Saturn's magnetosphere. They also emphasize the critical role of the 5–10 R_S region as a transition zone for both plasma composition and dynamics. Our results refine previous CAPS-based studies and underscore the need to incorporate seasonal variability and ionospheric coupling into future global models of Saturn's plasma environment.

1. Introduction

Saturn's magnetosphere is a uniquely neutral-rich environment, a defining characteristic that distinguishes it from most other planetary magnetospheres. It is also the second largest cohesive magnetic structure in our heliosphere, exceeded only by Jupiter's. A dominant contributor to these neutral populations is Enceladus, whose subsurface geological activity vents enormous amounts of water vapor through fissures in the south polar ice shell. High-velocity plumes eject water molecules at rates sufficient for much of the material to escape Enceladus' gravity and disperse directly into Saturn's magnetosphere (Brown et al., 2006; Dougherty et al., 2006; Hansen et al., 2006; Jones et al., 2006; Porco et al., 2006; Spahn et al., 2006; Spencer et al., 2006; Tokar et al., 2006; J. H. Waite et al., 2006). These plumes are known to extend up to ∼15,000 km from Enceladus' surface based on Cassini Ion Neutral Mass Spectrometer (J. Waite et al., 2004) observations (H. Smith et al., 2010), which was also recently confirmed by the James Webb Space Telescope Near-Infrared Spectrograph (Bagnasco et al., 2007; Gardner et al., 2006) observations to extend to nearly 10,000 km in altitude (Villanueva et al., 2023). Cassini's observations have also revealed that a strong signal of N^+ was detected near Enceladus, indicating that the water plumes are composed not only of H_2O, but also molecules that includes nitrogen (H. Smith et al., 2005, 2007, 2008).

Once injected, water plumes undergo physical chemistry interactions with solar photons and magnetospheric plasmas, becoming dissociated and ionized (as well as experiencing charge exchange), ultimately creating ion

© 2026. The Author(s).
This is an open access article under the terms of the Creative Commons Attribution License, which permits use, distribution and reproduction in any medium, provided the original work is properly cited.

21699402, 2026, 4, Downloaded from https://agupubs.onlinelibrary.wiley.com/doi/10.1029/2025JA034738 by Los Alamos National Laboratory, Wiley Online Library on [30/07/2026]. See the Terms and Conditions (https://onlinelibrary.wiley.com/terms-and-conditions) on Wiley Online Library for rules of use; OA articles are governed by the applicable Creative Commons License

products such as H^+, H_2^+, N^+, O^+, OH^+, H_2O^+, and H_3O^+ (Sittler et al., 2008; D. Young et al., 2005), which populate the entire magnetosphere of Saturn. This rotationally driven magnetosphere is powered by an immense plasma source from the moons and a strong electrodynamical coupling between the fast-rotating upper ionosphere of the planet and the fresh-born equatorial plasmas (Gombosi et al., 2009; T. W. Hill, 1979; Mauk et al., 2009).

Saturn's plasma environment was first directly explored in 1979 using in situ data obtained by the quadrispherical plasma analyzer (McKibbin et al., 1977) on Pioneer 11 (Hall, 1974), which measured the energy-per-charge (E/Q) of ions from 100 eV/q to 18 keV/q and electrons from 1 to 500 eV. Bulk plasma parameters such as number density, temperature, and flow speed were estimated by forward modeling of the measured E/Q distributions employing convected Maxwell-Boltzmann distribution functions assuming a set of ion species with mass-per-charge (M/Q) of 1, 2, 4, 8, 16, and 32 amu/q. It was concluded that the dominant ion species were O^+ or OH^+, for which a possible source was considered as a Saturn's icy ring system (Wolfe et al., 1980). The Voyager 1 and 2 spacecraft (Kohlhase & Penzo, 1977) encountered Saturn's magnetosphere in 1980 and 1981, respectively (e.g., Bridge et al., 1981, 1982) with the plasma science (PLS) instrument (Bridge et al., 1977) on Voyager providing E/Q measurements of ions and electrons from 10 eV/q to 5.95 keV/q. A comprehensive analysis of PLS ion data was conducted by Richardson (1986) and concluded that H^+ and O^+ are the dominant ion species and the source for O^+ located at ∼10 Saturn radii (1 R_S = 60,268 km), possibly originating from Titan, Rhea, and Dione.

While studies based on in situ measurements of plasma instruments on Pioneer 11, Voyager 1 and 2 have provided important insights into magnetospheric dynamics at Saturn, unique ion species identification was not possible because both instruments only provided E/Q measurements and lacked mass-per-charge measurements. Also, these missions were single-flyby encounters and thus the observations were limited spatially and temporally. The breakthrough in understanding ion composition at Saturn's magnetosphere occurred in 2004 when Cassini (Matson et al., 2002), the first Saturn-orbiting spacecraft, arrived at Saturn for its dedicated investigations. Cassini carried the Cassini Plasma Spectrometer (CAPS, Young et al., 2004), which comprised of three sensors: the Electron Spectrometer (ELS), the Ion Beam Spectrometer (IBS), and the Ion Mass Spectrometer (IMS). The IMS sensor measured both E/Q and M/Q through the time-of-flight technique, which allowed better ion species identification.

To date, the properties of the neutral component of water plumes have been extensively studied using Ion Neutral Mass Spectrometer data (Perry et al., 2015; J. H. Waite et al., 2006, 2009), and the bulk plasma properties of the major constituents (H^+, H_2^+, W^+, where W^+ represents the sum of the water-group ion species) have been addressed by several studies using CAPS data (e.g., Livi et al., 2014; Thomsen et al., 2010; Tokar et al., 2008; Wilson et al., 2017). However, the bulk plasma properties of the individual water group ion species (i.e., O^+, OH^+, H_2O^+, and H_3O^+) have not yet been studied well due to the relatively coarse mass resolution (M/ΔM ∼8) to resolve species with similar M/Q (∼16–19 amu/q). Even though preliminary studies on individual water group ions have been presented and have provided important insights (e.g., Felici, 2016; Felici et al., 2018; Wilson et al., 2015), the in situ bulk plasma properties, especially the number density and the temperature, of individual water group ions were still not well determined. Fleshman et al. (2010, 2012) have assessed the radial transport rate and physical chemistry of individual water group ions based on the preliminary composition obtained by CAPS (Tokar et al., 2006; D. Young et al., 2005). However, more statistically significant and explicit in situ composition analysis is required to precisely constrain the physical chemistry processes in the vicinity of Enceladus and the radial transport rate of dissociated water group ions.

Understanding the relative density ratio of individual water group ions (O^+, OH^+, H_2O^+, and H_3O^+) provides critical insights into heavy ion dynamics in Saturn's magnetosphere. The water group species dominate the ion dynamic processes occurring within the magnetosphere as they are one of the most abundant ions at Saturn (Thomsen et al., 2010). In rotationally driven magnetospheres such as Jupiter and Saturn, heavier ions are the dominant contributors to the thermal pressure and represent the bulk of total plasma energy (Bagenal & Delamere, 2011). This is because the entire magnetospheric plasma is subjected to corotation; therefore, large centrifugal forces confine the plasma in the equatorial plane, which affects the distribution along the magnetic field toward higher latitudes (T. Hill & Michel, 1976). Thus, analyzing their individual plasma properties is crucial in understanding global magnetospheric dynamics (e.g., sources, sinks, and radial transport) in Saturn's space environment.

CAPS is the only instrument on Cassini that can uniquely provide in situ data for computing bulk plasma properties such as flow speed, temperature, number density, and relative ion composition. Ion species

21699402, 2026, 4, Downloaded from https://agupubs.onlinelibrary.wiley.com/doi/10.1029/2025JA034738 by Los Alamos National Laboratory, Wiley Online Library on [30/07/2026]. See the Terms and Conditions (https://onlinelibrary.wiley.com/terms-and-conditions) on Wiley Online Library for rules of use; OA articles are governed by the applicable Creative Commons License

identification is accomplished by time-of-flight (TOF) determination with energy-per-charge (E/Q) measurement. However, it is challenging to resolve individual water group ions CAPS data as these ions have similar mass-per-charge (M/Q) such that the overlap of individual ion species is significant in both the Linear Electric Field (LEF), and Straight Through (ST) TOF detector subsystems. For this reason, water group ions have mostly been treated as a single ion species in previous studies based on CAPS data.

The difficulties in distinguishing water group ions from the CAPS TOF data can now be addressed by using newly calibrated TOF model functions for individual ion species. These were obtained from recent studies of a combination of in-flight and laboratory calibrations and instrument modeling, as documented in the Smith et al. (2019). In this study, we analyze entire CAPS TOF-ST data from mid-2004 to mid-2012, directly forward modeling the E/Q-TOF spectra for ion species such as H^+, H_2^+, N^+, O^+, OH^+, H_2O^+, and H_3O^+, utilizing convected kappa distributions (Olbert, 1968; Vasyliunas, 1968) similar to the techniques employed for Jupiter's magnetosphere (Kim et al., 2020a, 2020b). We present the first fully resolved global ion composition (i.e., number density ratio) and its associated thermodynamic plasma parameters, such as values of temperature, flow speed, and thermodynamic kappa, which further advance our current understanding of plasma dynamics in Saturn's magnetosphere. Section 2 presents an overview of the CAPS TOF data, Section 3 describes the forward modeling technique, Section 4 presents analysis results, and Section 5 discusses our findings.

2. Instrumentation and Data

In this section, we briefly discuss the CAPS-IMS sensor and provide data sets. The CAPS-IMS sensor comprises an electrostatic analyzer and a carbon foil-based TOF mass spectrometer. The sensor has an instantaneous field-of-view of 11° by 160° and it is mounted on a physical actuator to measure ion/electron distributions over ∼2π sr on a 3-axis stabilized spacecraft (D. Young et al., 2004). The instrument has an energy sweep cycle of 4 s with its resolution of $\Delta E/E \sim 0.17$ and capable of distinguishing ions with mass ranging from 1 to 60 amu/q with mass resolution of $M/\Delta M \sim 8$ for the ST and $M/\Delta M \sim 60$ for the LEF.

Due to limited telemetry, most of the data were telemetered back to Earth at different cadences: singles (SNG) data at multiples of 4-s cadence, and TOF data at multiples of 128-s cadence. Although both data types were measured simultaneously, they were transmitted separately and preserve different information. SNG data retain energy-per-charge (E/Q) measurement and directional information, while TOF data preserve E/Q and TOF measurements for rough ion species identification but lack directional information.

The TOF data are provided in two types: TOF-ST and TOF-LEF. The TOF-ST data are similar to those obtained from conventional TOF instruments (e.g., Wüest, 1998), measuring TOF from the time difference between the start signal generated from secondary electron emission released when ions transit through the foil (Ritzau & Baragiola, 1998) and the stop signal generated from particles that exited the foil, mostly neutral but small fraction being negatives and/or positives depending on the atomic species and their energy-per-nucleon (e.g., Kallenbach et al., 1993, 1995). In contrast, TOF-LEF data are obtained from a longer flight path and include only ions that remain positively charged after traversing the foil (see also McComas et al., 1990). The longer flight path yields significantly improved mass resolution compared to TOF-ST. However, because most ions become neutral after passing through the foil, only a small fraction of ions that retain positive charge are electrostatically deflected to the LEF detector, resulting in substantially lower detection efficiency than TOF-ST. Also, since the LEF is designed to measure TOF of ions after the foil regardless of energy of the atom after the foil, molecular ions would be measured as fragmented atomic ions, making it difficult to determine the true measured molecular ion species before it fragmented when passing through the foil.

Figure 1 shows an example of TOF-ST (top) and TOF-LEF (bottom) spectra taken during the same instances. The TOF-ST measured ions that became neutral and negative after traversing the carbon foil and the TOF-LEF measured only those that remained positive after traversing the foil. Since the majority of the ions become neutral, the detection efficiency for TOF-LEF is ∼10 times lower than that for TOF-ST. It has also been shown that the TOF-ST measures molecular ions as a whole, whereas TOF-LEF can only measure fragmented ions because the probability of the fragments recombining after the transit through the foil is extremely low (Funsten et al., 1994). As the Cassini mission had limited telemetry, the TOF-LEF data were predominantly telemetered within the TOF range shown in Figure 1, which does not preserve H^+ measurement.

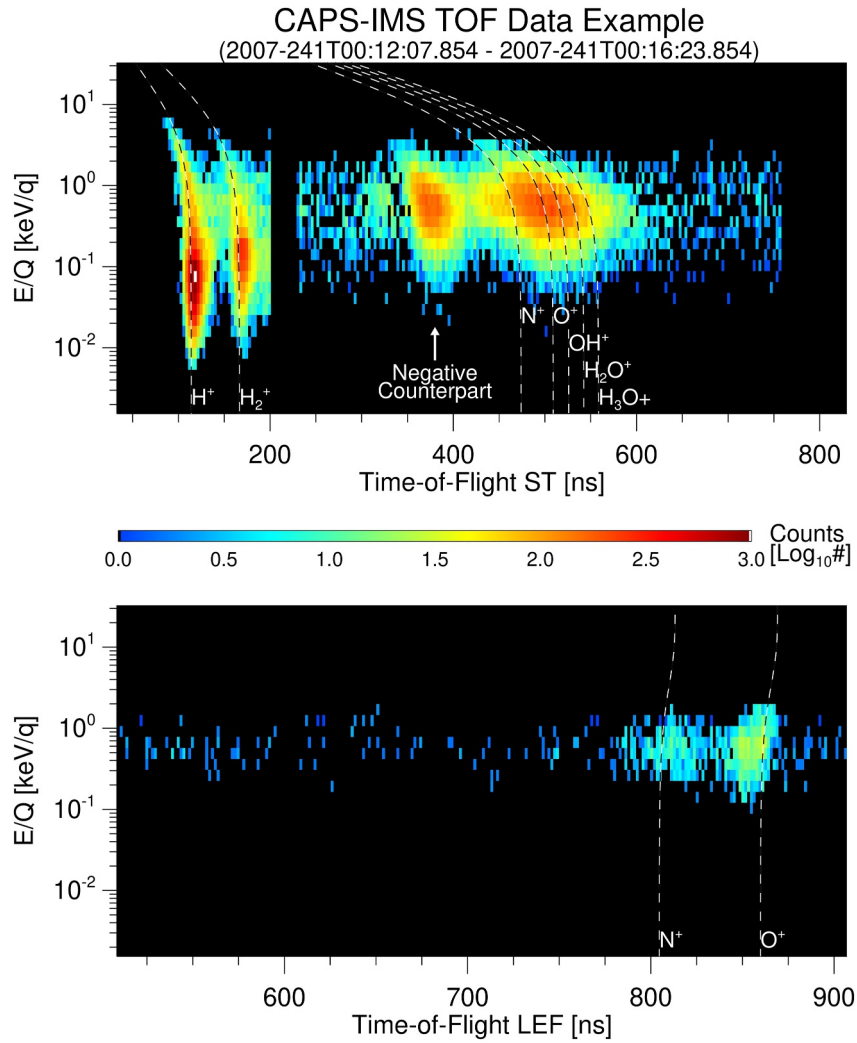


Figure 1. Example of CAPS-IMS TOF-ST (top) and TOF-LEF (bottom) data taken from 2007-241T00:12:07.854 to 2007-241T00:16:23.854 ($R = 8.96$ R_S, Latitude = 0.17°). Strong signals for H^+, H_2^+, N^+, O^+, OH^+, H_2O^+, and H_3O^+ are shown in TOF-ST spectra for the same interval. TOF-LEF spectra were only telemetered in the heavy ion TOF range due to the limited telemetry.

While TOF-ST data were collected for the full mass range from 1 to 60 amu/q in space, it was compressed to 128, 256 or 512 TOF bins from native 2048 bins and their full 63 energy tables were compressed into 32 energy tables due to limited telemetry (see Wilson et al., 2012).

Although the TOF-ST data have coarser mass resolution, the measured TOF preserves molecular ion species M/Q information. Therefore, the TOF-ST is the appropriate data for analyzing the individual water group ion species as molecular ion species are present in Saturn's magnetosphere. Another reason why TOF-LEF is not adequate for analyzing entire magnetospheric ions is that they were only telemetered for heavy ion measurement restricting analysis on H^+ and H_2^+ in addition to its limited information on measured molecular ion species (H. Smith et al., 2019).

Figure 2 provides an overview of CAPS-IMS TOF-ST data measured after the Saturn orbit insertion of the Cassini spacecraft. Top row shows average counts and bottom row shows time of Cassini orbit. The left column shows equatorial projections (local time) and the right column shows a meridional (side) view in kronocentric radial-theta-phi (KRTP) coordinate system, with a bin size of 0.5 Saturn radii (R_S). The KRTP system is defined as the x-axis pointing from Saturn toward the Sun, the z-axis is aligned with Saturn's north spin axis (which is

21699402, 2026, 4, Downloaded from https://agupubs.onlinelibrary.wiley.com/doi/10.1029/2025JA034738 by Los Alamos National Laboratory, Wiley Online Library on [30/07/2026]. See the Terms and Conditions (https://onlinelibrary.wiley.com/terms-and-conditions) on Wiley Online Library for rules of use; OA articles are governed by the applicable Creative Commons License

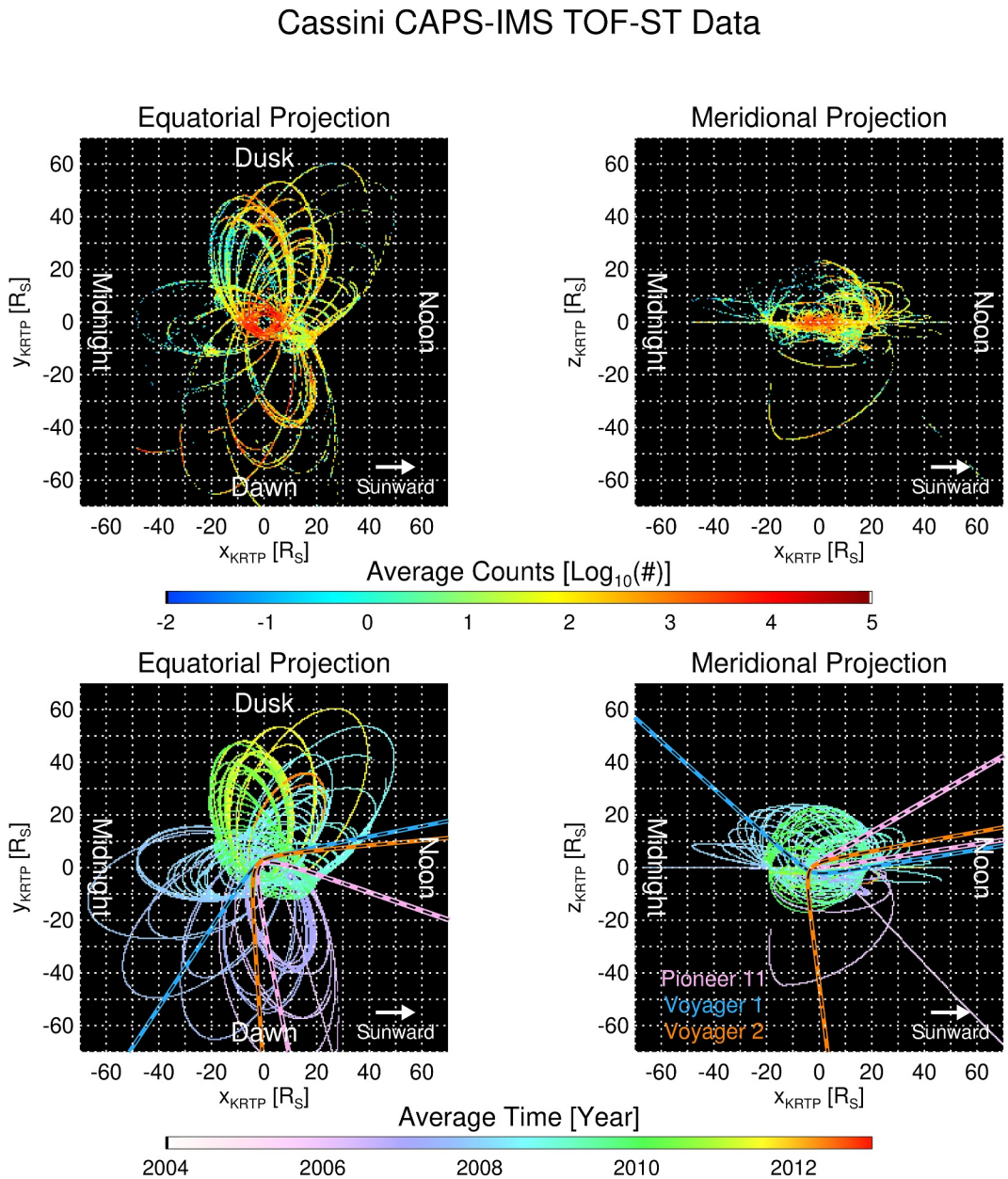


Figure 2. Average ion counts (top row) and time of observations (bottom row) made by Cassini CAPS-IMS are shown. The left column shows a top-down view of CAPS-IMS observations in local time, while the right panels provide a meridional (side) view. CAPS-IMS collected data in Saturn's magnetosphere from mid-2004 to mid-2012. The trajectories of Pioneer 11, Voyager 1, and Voyager 2 are shown with thick solid lines in magenta, blue, and orange, respectively. All coordinates shown here are in kronocentric radial-theta-phi (KRTP) coordinates.

identical to the magnetic dipole axis), and the y-axis completes a right-handed system, given by $\hat{y} = \hat{z} \times \hat{x}$. As shown in Figure 2, CAPS-IMS collected TOF-ST data from mid-2004 to mid-2012 in Saturn's magnetosphere with excellent local time, radial, and latitudinal coverage.

Figure 3 shows an example of average TOF-ST spectra measured near Saturn's equatorial plane (defined as x-y plane in KRTP coordinates, equatorial plane that's perpendicular to the Saturn's spin axis) from 3 to 15 R_S. Near Enceladus (located ~4 R_S), heavy ion counts are concentrated at low E/Q (peaking at approximately 0.14 keV/q, as indicated by horizontal lines in Figure 3) with a wide TOF distribution. As these plasmas are transported away

21699402, 2026, 4, Downloaded from https://agupubs.onlinelibrary.wiley.com/doi/10.1029/2025JA034738 by Los Alamos National Laboratory, Wiley Online Library on [30/07/2026]. See the Terms and Conditions (https://onlinelibrary.wiley.com/terms-and-conditions) on Wiley Online Library for rules of use; OA articles are governed by the applicable Creative Commons License

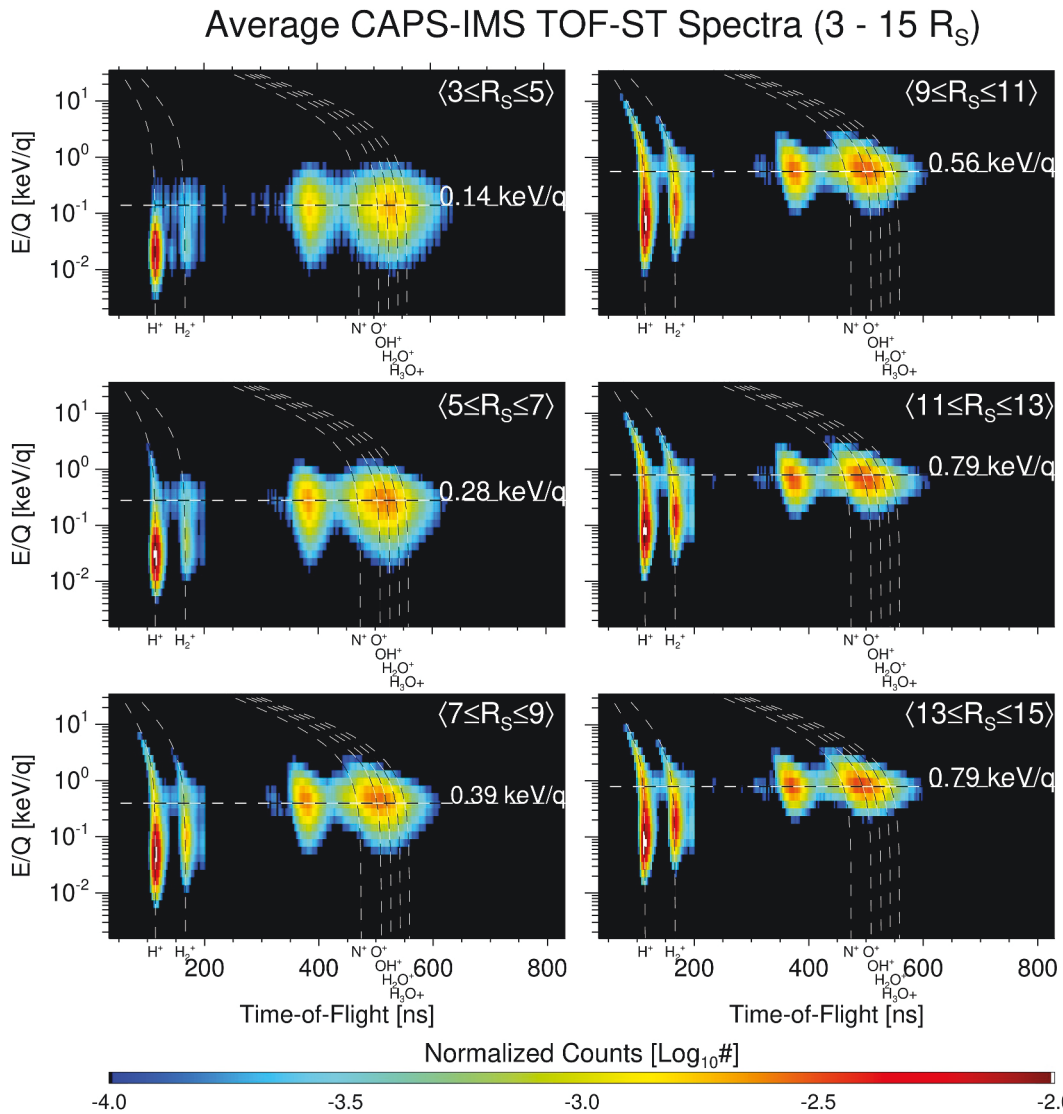


Figure 3. Average TOF-ST spectra from 3 to 15 R_S, within ±1.5 R_S from the equatorial plane (x-y plane in KRTP coordinates). Counts are normalized to the total counts in each TOF-ST spectra. A rough corotation E/Q is indicated by horizontal lines and texts, increasing with radial distance from Saturn. TOF-ST count peaks at relatively higher TOF (considerably higher TOF than where O^+ peak is expected) when data were collected near Enceladus (located at ~4 R_S) compared to the data collected farther away.

from the Enceladus, their counts become concentrated at higher E/Q (up to 0.79 keV/q) with a relatively narrower TOF distribution.

The counts observed in the TOF range of 300–350 ns are attributed to false start signals generated by H^-, rather than true start signals from secondary electron emissions from the carbon foil. If these counts represented real ions, they would correspond to species significantly lighter than C^+; however, no such ions are not identified in the TOF-LEF spectra. This interpretation is further supported by the absence of corresponding signatures in measurements from the Cassini Magnetospheric Imaging Instrument (MIMI, Krimigis et al., 2004)/Charge Energy Mass Spectrometer (CHEMS) and INMS (J. Waite Jr et al., 2004). Therefore, TOF ranges associated with H^- are excluded from our analysis.

21699402, 2026, 4, Downloaded from https://agupubs.onlinelibrary.wiley.com/doi/10.1029/2025JA034738 by Los Alamos National Laboratory, Wiley Online Library on [30/07/2026]. See the Terms and Conditions (https://onlinelibrary.wiley.com/terms-and-conditions) on Wiley Online Library for rules of use; OA articles are governed by the applicable Creative Commons License

3. Methodology

In this section, we introduce our methodology for obtaining ion properties via forward modeling of the in situ CAPS-IMS TOF-ST spectra. The methodology presented in this study follows the methodology presented by Kim et al. (2020a, 2020b) but is optimized for CAPS-IMS TOF-ST data and Saturnian ion species. The TOF-ST data is derived from multiple azimuthal scan (on the plane of actuator) with instantaneous field-of-view of 160° × 11° (20° × 11° per anode) covering roughly a hemisphere (2π sr). Then, the hemispherical TOF-ST counts can be written as follows, using counts to phase space density conversion,

$$C_i(E) = \Sigma_{j,k} c_i\left(E, \theta_l, \phi_m\right) = \Sigma_{j,k} 4 \cdot G(E) \cdot \varepsilon_i(E) \cdot E^2 \cdot \frac{f_i\left(E, \theta_j, \phi_k\right)}{m_i^2} \cdot \tau(E), \tag{1}$$

where C is total counts measured within accumulation time τ, i designates individual ion species, $G(E[\mathrm{eV}]) = 0.00427 + 0.00169 \cdot \left(\frac{E[\mathrm{eV}]}{1,000}\right)^{-0.1379} \cdot 10^{-4}\ \mathrm{m}^2 \cdot \mathrm{sr} \cdot \mathrm{eV}/\mathrm{eV}$ is the geometric factor for all 8 anodes, ε is the detection efficiency for TOF-ST which differs by individual ion species (H. Smith et al., 2019), f is the phase space density, E is the CAPS-IMS TOF-ST energy table, m is the target ion's mass. Indices j and k designate the anode number and the azimuthal scan number driven by the actuator. The angles are defined such that θ is measured perpendicular to the plane of the actuator's motion, and ϕ measured along with the actuator's direction of motion. The factor of 4 in Equation 1 is higher by a factor of 2 compared to typical counts to phase space density equation because a different definition is used for the CAPS-IMS geometric factor (see pg. 163–164 in Wilson et al., 2012 for details).

We choose the phase space density f for individual ion species to be a kappa distribution, a non-thermal generalization of Maxwell-Boltzmann distribution (e.g., Livadiotis, 2017; Livadiotis & McComas, 2013; Pierrard & Lazar, 2010), written as a function of CAPS-IMS energy table value E,

$$f(E, \delta) = n\left[\pi\left(\kappa - \frac{3}{2}\right)\eta^2\right]^{-\frac{3}{2}} \cdot \frac{\Gamma(\kappa+1)}{\Gamma\left(\kappa - \frac{1}{2}\right)} \cdot \left[1 + \frac{E + E_f - 2\sqrt{E}\sqrt{E_f}\cos\delta}{\left(\kappa - \frac{3}{2}\right)k_B T}\right]^{-\kappa-1} \tag{2}$$

where n is ion number density, κ is the thermodynamic kappa, k_B is Boltzmann constant, and T is ion's temperature, $\eta = \sqrt{\frac{2k_B T}{m}}$ is thermal speed, Γ is a gamma function, $E_f = \frac{1}{2}\mathrm{m}\mathrm{v}_f^2$ is ion bulk flow energy, and δ is the thermal spread angle between the individual ion velocity $\vec{v}$ and bulk flow vector $\vec{v_f}$. The thermodynamic kappa and temperature comprise the two intensive independent parameters that fully characterize the thermodynamics of the space plasma particle populations (Livadiotis, 2018; Livadiotis & McComas, 2023); the temperature provides the average kinetic energy per particle, while the kappa measures the correlations between the particle energies (Livadiotis & McComas, 2021).

Following the same derivation process shown in Kim et al. (2020a, 2020b), the equation for measured counts C at specific energy E for accumulated time of τ with common flow energy E_f for ion species i can be obtained below by integrating over the thermal spread angle $-\pi/2 \le \delta \le +\pi/2$, that is,

$$C_i(E) = \frac{n_i}{4}\sqrt{\frac{2}{m_i}} \cdot \left[\pi^3 E_f k_B T_i \left(\kappa_i - \frac{3}{2}\right)\right]^{-\frac{1}{2}} \cdot \frac{\Gamma(\kappa_i)}{\Gamma\left(\kappa_i - \frac{1}{2}\right)} \cdot \left\{\left[1 + \frac{E + E_f - 2\sqrt{E}\sqrt{E_f}}{\left(\kappa_i - \frac{3}{2}\right)k_B T_i}\right]^{-\kappa_i} - \left[1 + \frac{E + E_f + 2\sqrt{E}\sqrt{E_f}}{\left(\kappa_i - \frac{3}{2}\right)k_B T_i}\right]^{-\kappa_i}\right\} \cdot E^{\frac{3}{2}} G(E) \cdot \frac{N_A(E)}{8} \cdot \varepsilon_i(E) \cdot \tau, \tag{3}$$

21699402, 2026, 4, Downloaded from https://agupubs.onlinelibrary.wiley.com/doi/10.1029/2025JA034738 by Los Alamos National Laboratory, Wiley Online Library on [30/07/2026]. See the Terms and Conditions (https://onlinelibrary.wiley.com/terms-and-conditions) on Wiley Online Library for rules of use; OA articles are governed by the applicable Creative Commons License

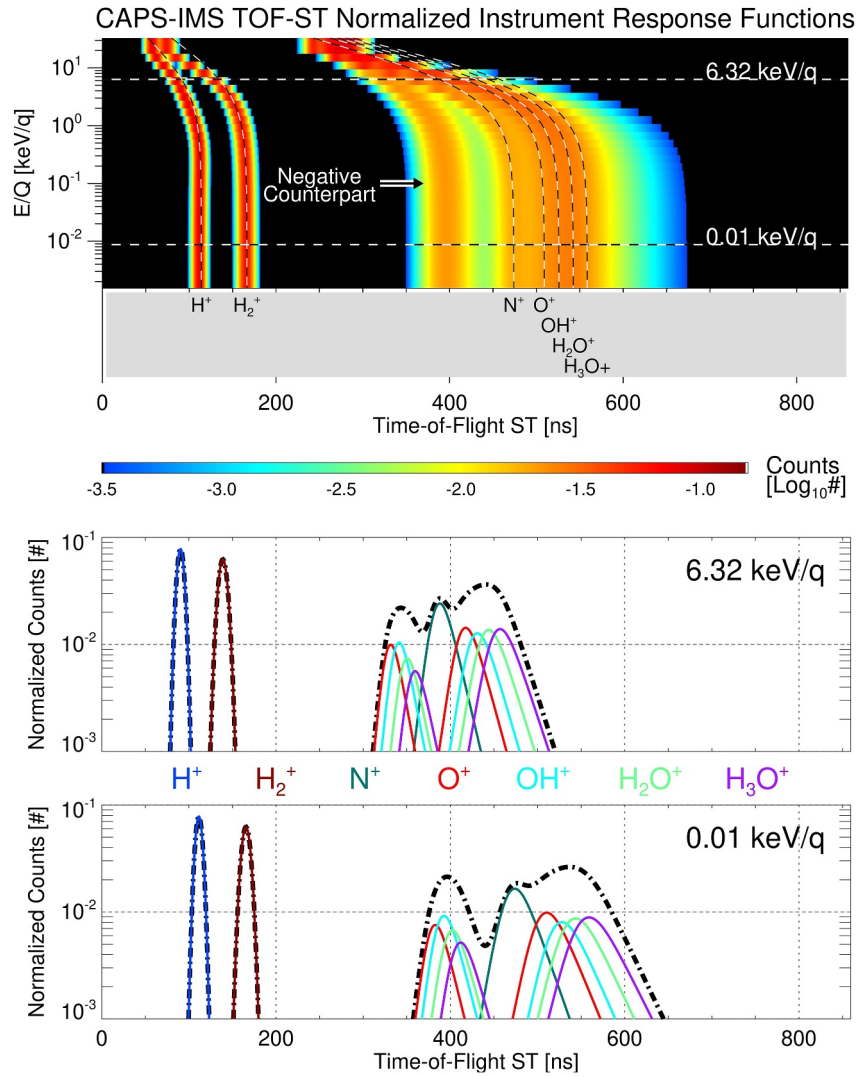


Figure 4. The top panel shows the E/Q-TOF spectra for the sum of normalized instrument response functions for the CAPS-IMS TOF-ST, with the total of individual functions equaling one count, for the following ions: H^+, H_2^+, N^+, O^+, OH^+, H_2O^+, H_3O^+. The bottom two panels show the TOF-ST distributions for energies of 6.32 keV/q and 0.01 keV/q, respectively. These instrument response functions are combined with generated E/Q distributions to obtain the forward-modeled E/Q-TOF spectra. Negative counterparts appear in the data due to charge state modification when ions interact with the ultrathin carbon foils, with the exception of N^+.

where N_A is the number of anodes that detect non-zero counts. The $N_A(E)$ parameter is calculated using SNG data collected during TOF data accumulation time, which are background subtracted and corrected for anode cross-talks based on the methods presented in Wilson et al. (2012). Since the TOF-ST geometric factor is just a factor of eight (i.e., number of anodes) times the SNG geometric factor, it needs to be scaled down based on the number of anodes that actually collect counts. We generate this scale factor for the 32 compressed energy steps.

In our forward model, we include seven ion species H^+, H_2^+, N^+, O^+, OH^+, H_2O^+, and H_3O^+. Although, CAPS clearly detected O_2^+ near Rhea and Dione (Martens et al., 2008; Tokar et al., 2012), we excluded it from our forward model as the signal to noise ratio was insufficient leading to the forward model to fit the remnant radiation background or false coincidences generated by water group ion species.

From Equation 3, we generate seven E/Q distributions for H^+, H_2^+, N^+, O^+, OH^+, H_2O^+, and H_3O^+ with provided τ, n, v for E_f, T, m, and κ for the native 63 energy channels. These are merged with normalized TOF-ST response functions to obtain ion species dependent plasma parameters. Figure 4 shows a normalized TOF-ST response

21699402, 2026, 4, Downloaded from https://agupubs.onlinelibrary.wiley.com/doi/10.1029/2025JA034738 by Los Alamos National Laboratory, Wiley Online Library on [30/07/2026]. See the Terms and Conditions (https://onlinelibrary.wiley.com/terms-and-conditions) on Wiley Online Library for rules of use; OA articles are governed by the applicable Creative Commons License

21699402, 2026, 4, Downloaded from https://agupubs.onlinelibrary.wiley.com/doi/10.1029/2025JA034738 by Los Alamos National Laboratory, Wiley Online Library on [30/07/2026]. See the Terms and Conditions (https://onlinelibrary.wiley.com/terms-and-conditions) on Wiley Online Library for rules of use; OA articles are governed by the applicable Creative Commons License

function for the native 63 energy channels and 2048 TOF-ST bins that were recently modified based on empirical model functions described by Smith et al. (2019). The modification was based on in situ TOF-ST spectra where the clearly separated signal for O^+ was visible in the outer magnetosphere (see Appendix for details).

We assume a common flow speed for all ion species and a common kappa value and temperature for heavy ions (i.e., N^+, O^+, OH^+, H_2O^+, and H_3O^+) as heavy ions are expected to reach thermal equilibrium by the time they are transported away from the source region (i.e., Enceladus). Therefore, the forward model presented in this study finds 14 plasma parameters (ion number densities $n(H^+)$, $n(H_2{}^+)$, $n(N^+)$, $n(O^+)$, $n(OH^+)$, $n(H_2O^+)$, $n(H_3O^+)$, 1-D flow speed v_f in spacecraft frame, temperatures $T(H^+)$, $T(H_2{}^+)$, $T(W^+)$, and kappa $\kappa(H^+)$, $\kappa(H_2{}^+)$, $\kappa(W^+)$. We exclude the spacecraft speed term in our forward model as its value is typically very small (<10 km/s) compared to the flow speed (ranging from ~10 km/s to ~100 km/s).

Within each single B-cycle TOF-ST record, the compression of TOF bins from 2048 to either 128, 256, or 512 often changed, which caused a shift in the peak of the distribution for different ion species (see Wilson et al., 2012). Therefore, we introduced a TOF shifting parameter for all ion species and all energy steps, which add up to a total of 15 free parameters in the forward model. These parameters are found by minimizing the chi-squared value defined as,

$$\chi^2 = \sum_{E=1}^{32} \sum_{\mathrm{TOF}=1}^{128,256,512} \frac{[\mathrm{Data}(E,\mathrm{TOF}) - \mathrm{Model}(E,\mathrm{TOF})]^2}{\sigma^2_{\mathrm{Total}}(E,\mathrm{TOF})}, \tag{4}$$

where Data is the background subtracted TOF-ST data (see Smith et al., 2019 for background subtraction method) and σ_{Total} is the statistical uncertainty for the background-subtracted data expressed as

$$\sigma_{\mathrm{Total}}(E,\mathrm{TOF}) = \sqrt{\sigma^2_{\mathrm{Data}}(E,\mathrm{TOF}) + \sigma^2_{\mathrm{Bgrd}}(E,\mathrm{TOF})}. \tag{5}$$

We first generate modeled TOF-ST in full resolution with 63 energy steps and 2,048 TOF bins and then compress it to the resolution of individual telemetered TOF-ST data (typically 32 energy channels by 128/256/512 TOF-ST bins) for calculating a chi-squared value. The TOF shifting parameter is introduced after the compression. Also, there were cases when data was missing in certain energy steps for a given TOF-ST record. We removed those incomplete data from the forward model process.

Figures 5 and 6 show forward model examples for two cases: one at a closer distance to Enceladus (4.29 R_S) and the other at a farther distance (8.60 R_S). In Figure 5, the TOF-ST distribution is substantially broader in TOF, reflecting the dominance of molecular ions near Enceladus. By contrast, Figure 6 shows a much narrower overall TOF distribution, as the population is primarily composed of atomic ion species. Since molecular ions are dominant close to Enceladus. In Figures 5 and 6, the top panel shows the in situ TOF-ST spectra, the middle panel shows the forward model spectra, and the bottom panel shows count-TOF distribution comparison at specific E/Q. In the bottom panels, in situ data are shown with black lines with gray error bars (representing Poisson statistics), and the forward model is shown with color-coded lines and dots. The magenta dots are the sum of forward modeled individual ion counts. Molecular ions clearly dominate near Enceladus.

We ran our forward model to individual B-cycle TOF-ST records that have total counts (accumulated over all energy and TOF-ST channels) greater than 2,000 that are only measured within Saturn's magnetosphere. This resulted in a total of 10,970 TOF-ST records that were forward modeled.

4. Results

This section presents the forward model results of all CAPS IMS TOF-ST B-cycle records that are available at the Planetary Data System/Planetary Plasma Interactions (PDS/PPI) node. We excluded unphysical results from the analysis, such as those with near-zero flow speed (also discussed in Thomsen et al., 2010) and low signal to noise records that were collected within Saturn's radiation belt. The analysis in this section includes 9,020 forward model samples with physically meaningful values out of a total of 10,970 forward model fits.

Of the 9,020 valid forward model fits, 58 were obtained during close moon flybys (within 10 moon radii), including Enceladus (20), Dione (9), Rhea (26), and Titan (3). The 10-moon-radii threshold follows the criterion

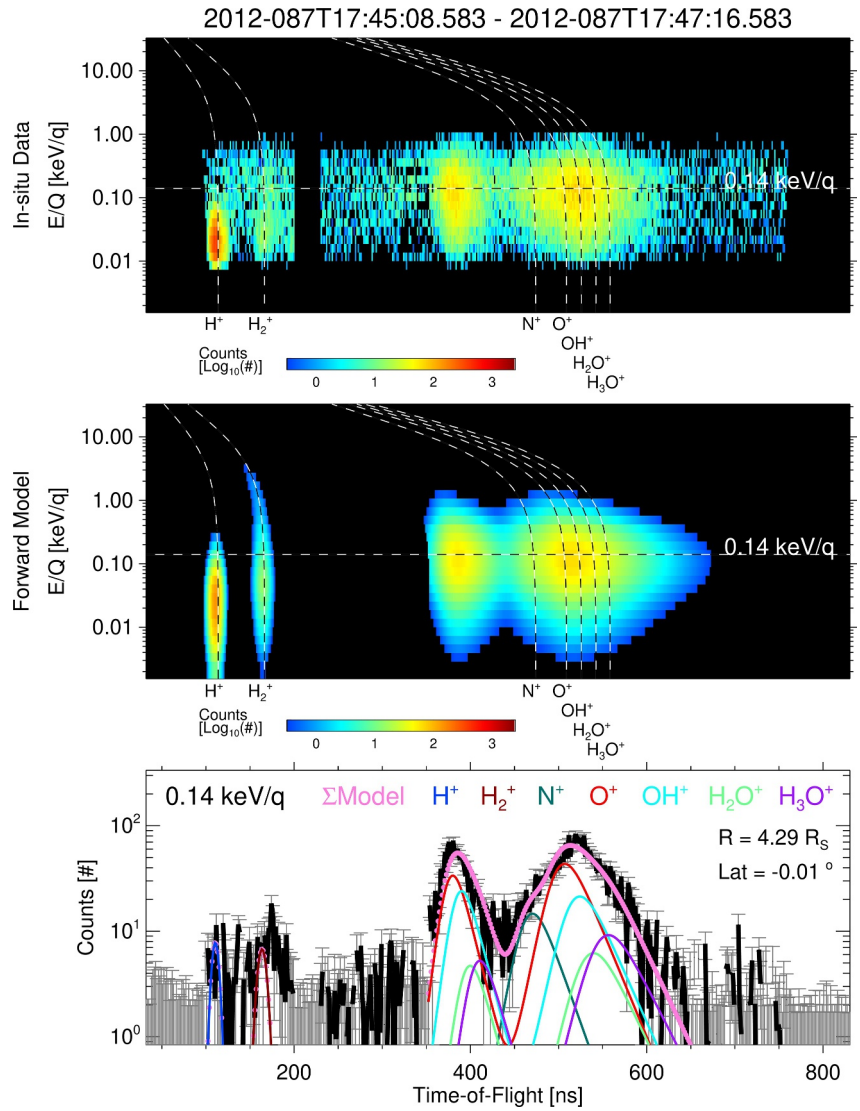


Figure 5. An example of a forward model for the data collected at 4.29 R_S. Top panel shows in situ TOF-ST spectra, middle panel shows forward model fit, and finally the bottom panel shows comparison of data (shown with black) and the model (color coded) at E/Q = 0.14 keV/q. A fair amount of molecular ions are observed at this distance.

adopted by Wilson et al. (2017). These intervals are excluded from the main analysis because moon-plasma interactions can significantly modify local plasma properties (e.g., Jia et al., 2010; Tokar et al., 2006, 2012).

Figure 7 summarizes the forward model results in KRTP coordinates, averaged (weighted by uncertainties of fit parameters) over all local times and binned in 1 R_S by 1 R_S. The *x*-axis represents the axial distance from the Saturn's rotation (or dipole magnetic) axis that is equivalent to ρ_{SPIN} and the *y*-axis shows the vertical distance from the equatorial plane. The magenta lines indicate the dipole magnetic field for L-shells of 2, 4, 6, 8, 10, 12, 14, and 16. The top-left panel shows the total number of forward model samples, indicating that most fits are concentrated within 10 R_S in the equatorial plane. The lower statistics at higher latitudes are largely due to the spacecraft's relatively low orbital inclination angle (see upper-right panel in Figure 2). Additionally, the CAPS instrument was turned off in 2012 before the proximal orbits (with high orbital inclination angle) due to a high voltage anomaly.

The flow speed, measured in the spacecraft frame (which closely approximates the plasma bulk flow since the spacecraft velocity is small), increases rapidly with distance from Saturn, reaching up to ~140 km/s at ~14 R_S. The number densities decrease rapidly with distance, except for H_2^+, which exhibits relatively smaller density

21699402, 2026, 4, Downloaded from https://agupubs.onlinelibrary.wiley.com/doi/10.1029/2025JA034738 by Los Alamos National Laboratory, Wiley Online Library on [30/07/2026]. See the Terms and Conditions (https://onlinelibrary.wiley.com/terms-and-conditions) on Wiley Online Library for rules of use; OA articles are governed by the applicable Creative Commons License

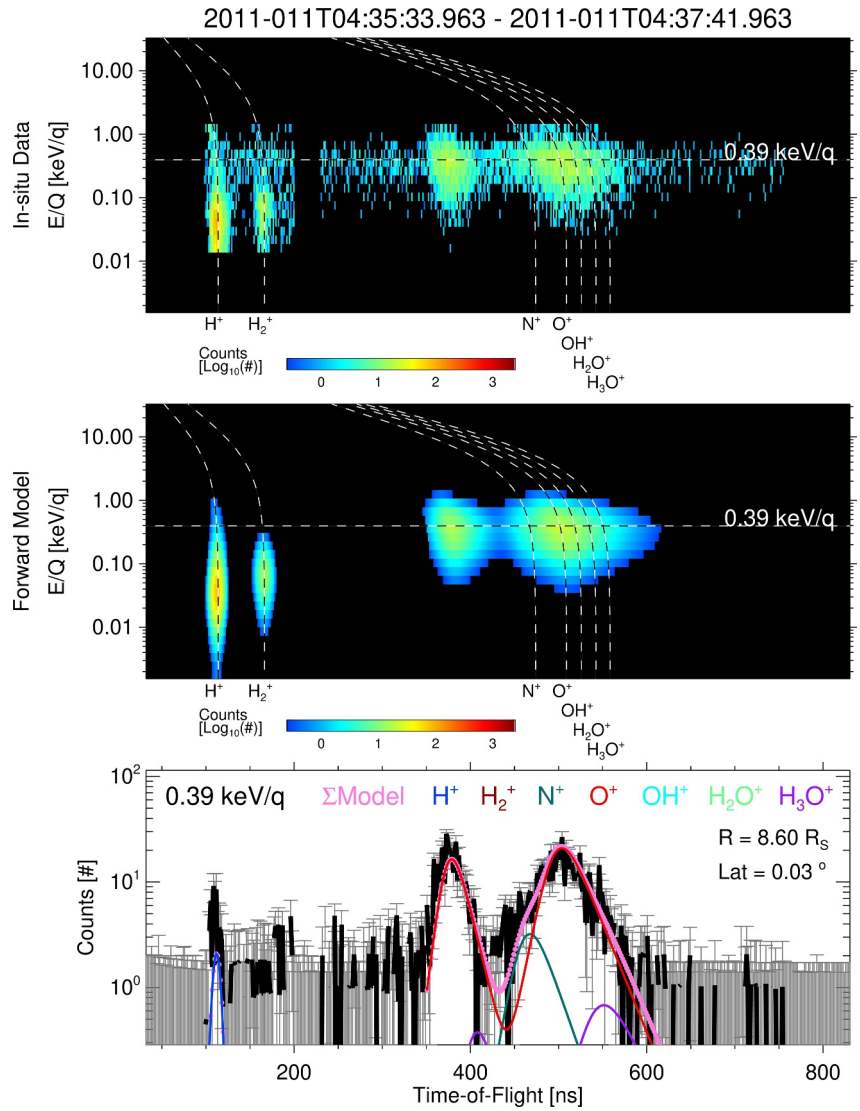


Figure 6. An example of a forward model for the data collected at 8.60 R_S. Same format as Figure 5. Molecular ions are notably reduced compared to the case shown in Figure 5.

variations compared to other ion species. The results indicate that heavy ions (N^+, O^+, OH^+, H_2O^+, and H_3O^+) dominate the Saturn's magnetosphere, primarily concentrated in the equatorial plane due to centrifugal force confinement (T. W. Hill, 1979). O^+ seems to be the most dominant ion species where its peak density is located around 5–6 R_S. OH^+ and H_3O^+ ions also show high number densities between 3 and 5 R_S where their peak density location is closer to Enceladus' orbital distance at ~4 R_S.

Ion temperature increases significantly with radial distance, with its value scaling approximately with ion mass. While both flow speed and temperature increase outward, the kappa decreases rapidly. The H^+ kappa exceeds 100 (plotted on a logarithmic scale) between 4 and 7 R_S, indicating a plasma distribution near the classical thermal equilibrium ($\kappa \rightarrow \infty$), which can be well described by a convected Maxwell-Boltzmann distribution (Livadiotis & McComas, 2011; Pierrard & Lazar, 2010). Beyond 7 R_S, the H^+ kappa values drop sharply. H_2^+ kappa values do not show a clear radial trend, with overall low values. The heavy ions (N^+, O^+, OH^+, H_2O^+, and H_3O^+) exhibit higher overall kappa indices compared to H^+ and H_2^+, with its highest kappa indices also observed between 4 and 7 R_S, coinciding with the peak location of the H^+ kappa value.

Figure 8 shows the latitudinally summed local time view (top-down perspective) of the forward model results. The model samples are relatively evenly distributed across the noon, dawn, and midnight sectors, but slightly

21699402, 2026, 4, Downloaded from https://agupubs.onlinelibrary.wiley.com/doi/10.1029/2025JA034738 by Los Alamos National Laboratory, Wiley Online Library on [30/07/2026]. See the Terms and Conditions (https://onlinelibrary.wiley.com/terms-and-conditions) on Wiley Online Library for rules of use; OA articles are governed by the applicable Creative Commons License

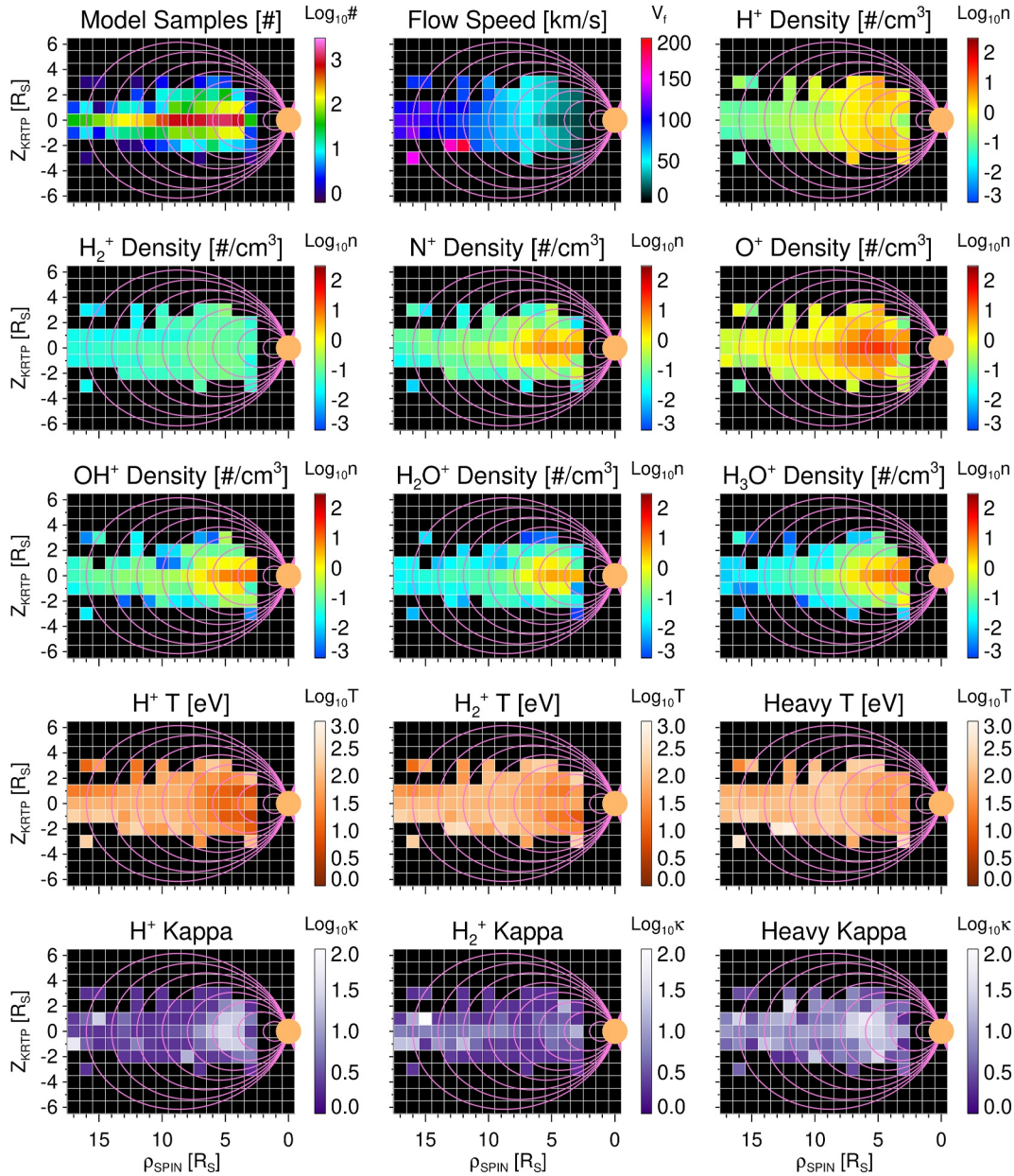


Figure 7. Forward model results averaged over all local times are shown in KRTP coordinates with a bin size of 1 × 1 R_S. All parameters are plotted on logarithmic scales, except for the flow speed, to highlight the radial and latitudinal variations. Magenta curves indicate dipole magnetic field lines at L-shells 2, 4, 6, 8, 10, 12, and 14. Density, temperature, and kappa panels each share a common colorbar scale across their respective sets, allowing direct comparison.

under-sampled near dusk. The flow speed increases with increasing radial distance at all local times. The number densities decrease rapidly as the plasma is transported outwards, with a clear dusk enhancement of H^+, N^+, O^+, H_2O^+, and H_3O^+, where OH^+ shows strong dawn enhancement. Ion temperatures increase with radial distance without showing any trend toward specific local time. The local time distribution of both H^+ ions and heavy kappa values is weakly asymmetric, with a modest enhancement toward the noon sector compared to other local times.

However, it is difficult to determine whether the observed trends in plasma parameters are truly local time-dependent, as the measurements were made at different times for each sector (see the bottom-left panel of Figure 2). We further discuss this issue in Section 5, exploring whether the observed trends result from temporal

21699402, 2026, 4, Downloaded from https://agupubs.onlinelibrary.wiley.com/doi/10.1029/2025JA034738 by Los Alamos National Laboratory, Wiley Online Library on [30/07/2026]. See the Terms and Conditions (https://onlinelibrary.wiley.com/terms-and-conditions) on Wiley Online Library for rules of use; OA articles are governed by the applicable Creative Commons License

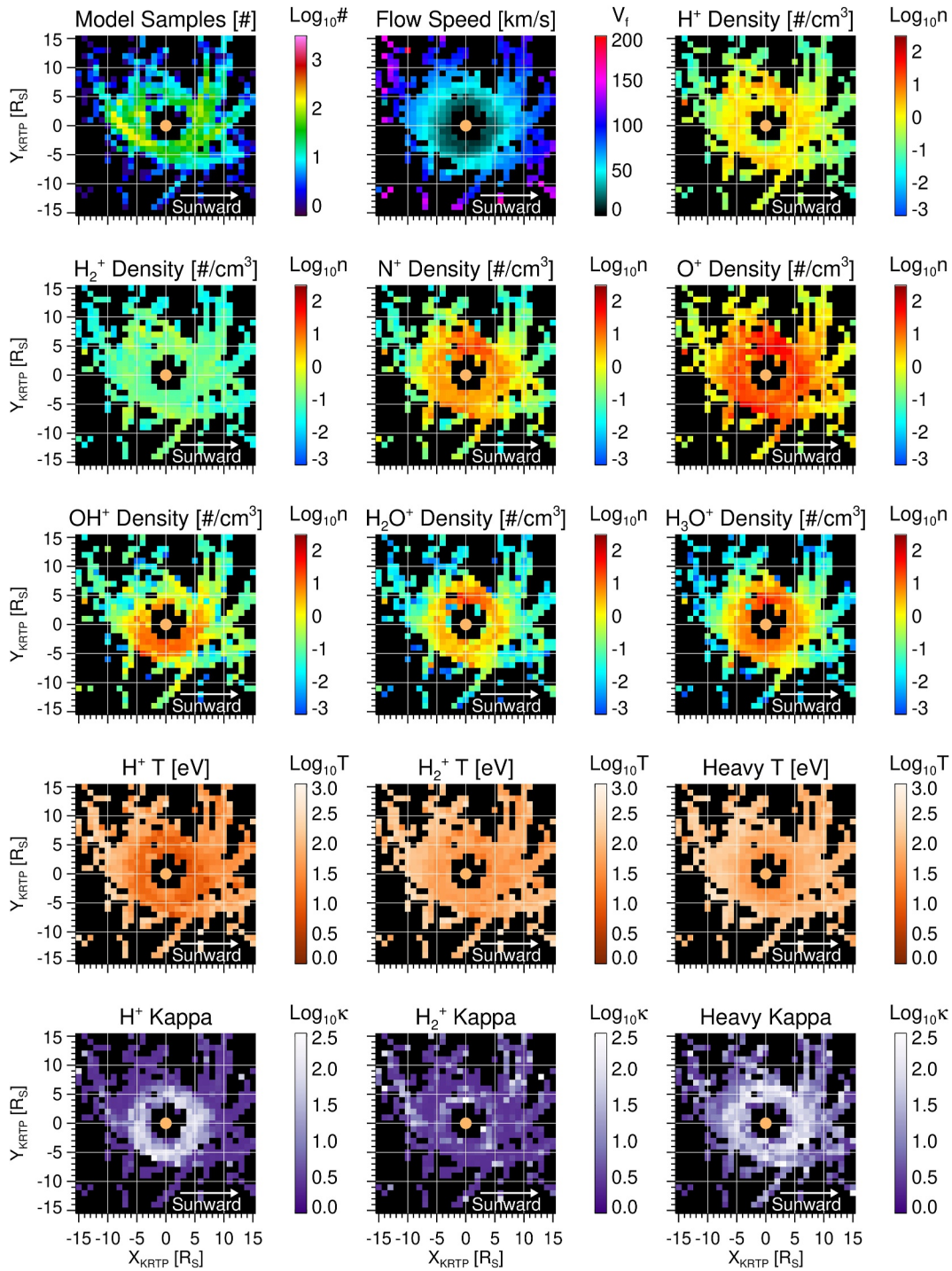


Figure 8. Same format as Figure 7 but showing latitudinal-averaged local time view (top-down perspective).

variations or the local time dependencies. In the following subsections, we examine individual plasma parameters in detail, comparing them with previous studies based on CAPS-IMS observations.

4.1. Flow Speed

Figure 9 shows 1-D flow speed as a function of ρ_{SPIN} and absolute latitude. Rigid corotation speeds are indicated by a solid white line. At a given ρ_{SPIN}, the flow speed tends to be higher at greater latitudes, occasionally even

21699402, 2026, 4, Downloaded from https://agupubs.onlinelibrary.wiley.com/doi/10.1029/2025JA034738 by Los Alamos National Laboratory, Wiley Online Library on [30/07/2026]. See the Terms and Conditions (https://onlinelibrary.wiley.com/terms-and-conditions) on Wiley Online Library for rules of use; OA articles are governed by the applicable Creative Commons License

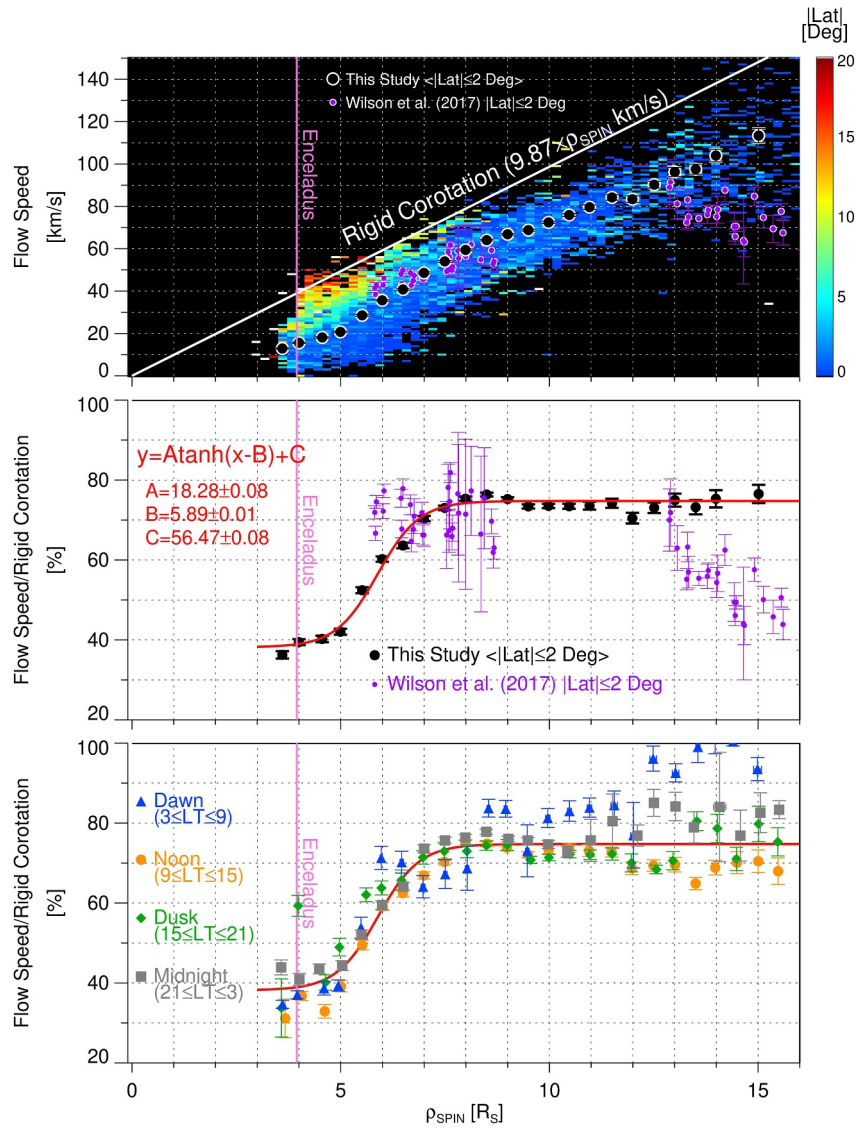


Figure 9. The 1-D flow speed from the forward model results is shown. The colors in the top panel represent the average of the absolute latitude values (relative to the x-y plane in KRTP coordinates). Solid white line indicates rigid corotation speed. The flow speed is 1-D, including radial, latitudinal, and longitudinal components, partly due to the limitations of TOF data (see Section 2). At high latitudes, the flow speed sometimes exceeds the rigid corotation speed, implying strong radial or latitudinal flows. For comparison, the flow speed Wilson et al. (2017) is shown with purple dots. Most error bars are comparable to or smaller than the symbol size. The second panel shows the flow speed relative to rigid corotation for all local times and the bottom shows the flow speed for each local time.

exceeding the rigid corotation speed, likely due to increased contributions from the radial and theta velocity components. To extract meaningful trends from the 1-D flow speed data, we computed average values within ±2° latitude of the equatorial plane, shown with black dots. Error bars represent the standard deviation of the mean and are typically comparable in size to the symbols.

For comparison with prior work, we include azimuthal flow speed (v_ϕ) derived from Wilson et al. (2017), shown as purple dots, within ±2° of latitude. Wilson et al. (2017) forward-modeled individual SNG data using double Maxwell-Boltzmann distribution, assuming that the ion population was composed solely of H^+ and OH^+. However, this assumption can introduce significant bias in flow speed estimates, as the derived speed depends on the average ion mass via the relation $E = 1/2\ mv^2$.

21699402, 2026, 4, Downloaded from https://agupubs.onlinelibrary.wiley.com/doi/10.1029/2025JA034738 by Los Alamos National Laboratory, Wiley Online Library on [30/07/2026]. See the Terms and Conditions (https://onlinelibrary.wiley.com/terms-and-conditions) on Wiley Online Library for rules of use; OA articles are governed by the applicable Creative Commons License

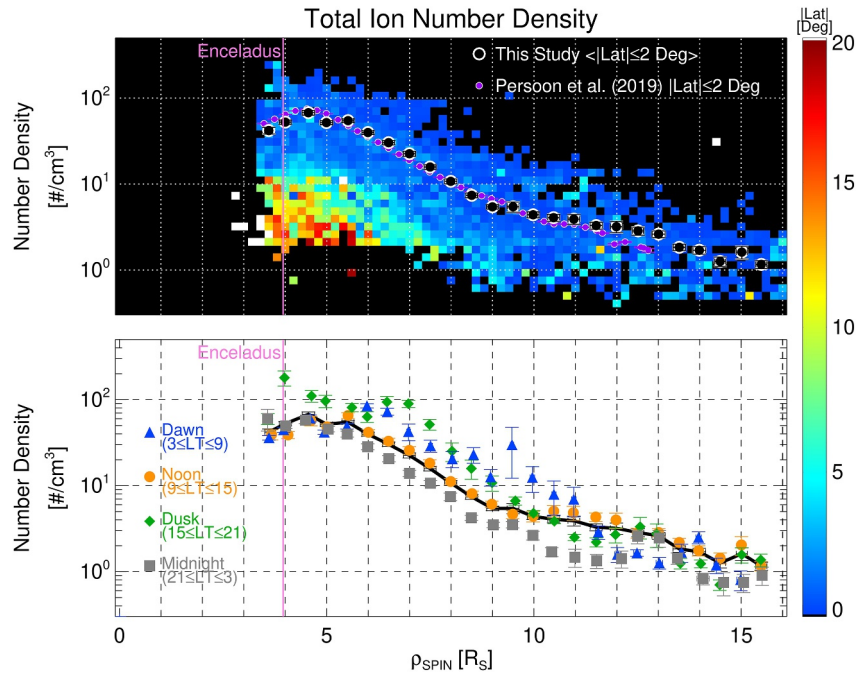


Figure 10. Radial profile of the total ion number density derived in this study. Black dots represent the average ion number density within ±2° latitude of the equatorial plane. Purple dots in the upper panel show the average RPWS-derived electron number densities within ±2° latitude of the equatorial plane (Persoon et al., 2019).

Our results from Figures 7 and 8 demonstrate that O^+ dominates beyond ~5 R_S, while OH^+ and H_3O^+ are more prevalent closer to Enceladus. This composition-dependent behavior is clearly reflected in the comparison shown in Figure 9. Results from Wilson et al. (2017) agree well with our values near ~8 R_S, but show higher flow speeds inside 8 R_S and lower speeds beyond that point. Because accurate flow speed estimation requires knowledge of the average ion mass, our identification of individual water group ion species using TOF-ST data provides the first direct constraint on this quantity.

To enhance the visibility of flow speed trends, the second panel of Figure 9 includes an empirical fit using a hyperbolic tangent function that describes the fractional flow speed relative to rigid corotation. This empirical relationship is valid only beyond 3 R_S, since plasmas rigidly corotate with Saturn within this distance (Wilson et al., 2009). The flow speed shows a rapid increase from ~40% to ~70% from 5 to 8 R_S, which coincides with the region where ion composition also rapidly changes. We discuss this matter in Section 5.

The third panel of Figure 9 shows the local time dependency of the equatorial flow speed. In general, the dawn and midnight sectors show higher flow speeds than the local time-averaged values. Notably, flow speeds in the dusk sector near Enceladus' orbital distance are approximately 20% higher than those at other local times, while the noon sector shows the lowest flow speeds. This local time dependence is discussed further in Section 5.

4.2. Number Densities

Figure 10 shows the total ion number density derived by summing the number densities of seven ion species-H^+, H_2^+, N^+, O^+, OH^+, H_2O^+, and H_3O^+. In the top panel, the black dots represent average number densities within ±2° latitude from the equatorial plane from this study. Purple dots are the average equatorial electron number densities derived from the RPWS instrument (Gurnett et al., 2004; Persoon et al., 2019). The RPWS-derived electron densities show good agreement with the total ion number densities obtained in this study.

The bottom panel shows the local time dependence of the total ion number density derived in this study. The dawn and dusk sectors show higher number densities than the local-time-averaged values, whereas the midnight sector shows lower densities. The highest number density is observed in the dusk sector near Enceladus' orbital distance, corresponding to the enhanced flow speeds observed in this region. In contrast, the noon sector is generally consistent with the local-time-averaged total ion number density.

21699402, 2026, 4, Downloaded from https://agupubs.onlinelibrary.wiley.com/doi/10.1029/2025JA034738 by Los Alamos National Laboratory, Wiley Online Library on [30/07/2026]. See the Terms and Conditions (https://onlinelibrary.wiley.com/terms-and-conditions) on Wiley Online Library for rules of use; OA articles are governed by the applicable Creative Commons License

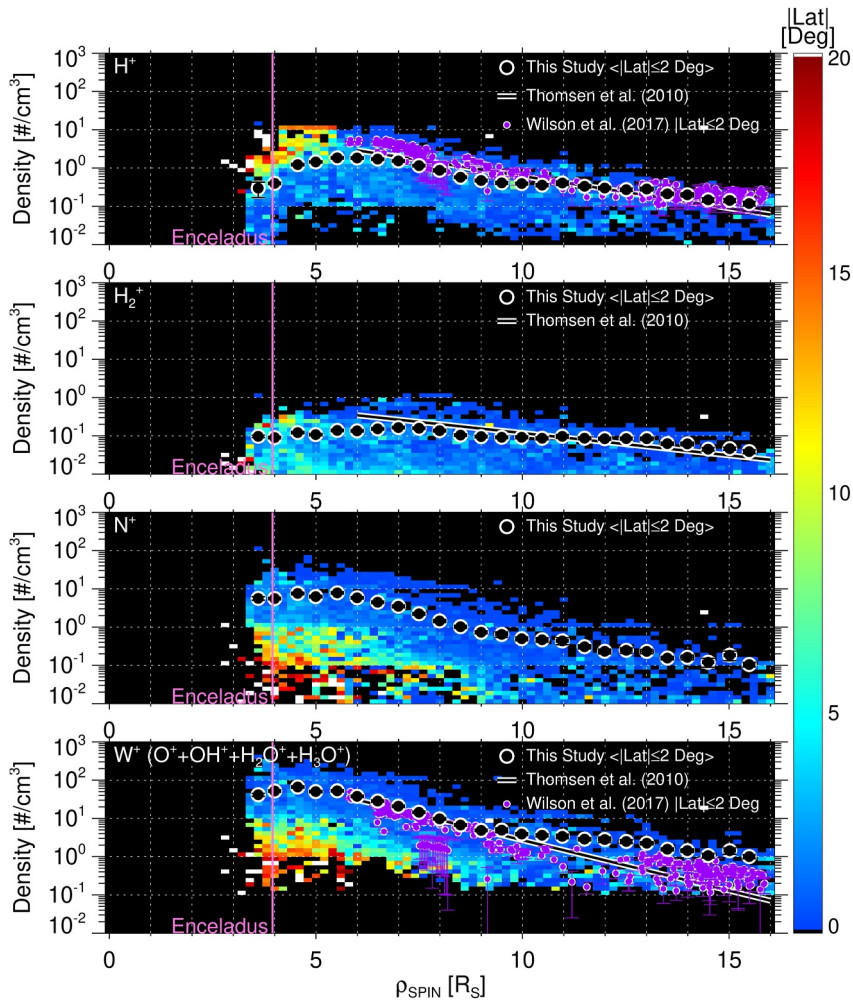


Figure 11. Ion number densities for H^+, H_2^+, N^+, and W^+ compared to previous studies. Black dots indicate the average number density values from this study within ±2° latitude of the equatorial plane. The color scale represents the average of the absolute latitude values. Error bars represent the standard deviation of the mean, and they are generally comparable to or smaller than the symbol size. For comparison, density values from Thomsen et al. (2010) are shown with solid lines and Wilson et al. (2017) with magenta dots.

Figure 11 shows the number densities of H^+, H_2^+, N^+, and W^+ (where $W^+ = O^+ + OH^+ + H_2O^+ + H_3O^+$), binned using the same approach as in Figure 9. All water group ions are grouped as W^+ to facilitate comparison with previous studies, as no prior work has derived number densities for the individual water group ion species. In each panel, black dots represent average number densities within ±2° latitude from the equatorial plane, with associated error bars indicating the standard deviation of the mean. Solid black lines represent empirical models (expressed in both power law and exponential fits) from Thomsen et al. (2010), and purple dots show results from Wilson et al. (2017) that are within ±2° latitude.

It is important to note that only Thomsen et al. (2010) provided results for H_2^+, and no previous studies reported number densities for N^+. H^+ densities are generally higher at higher latitudes, while N^+ and W^+ exhibit the opposite trend, with peak densities near the equatorial region. These findings support the expected centrifugal confinement of heavy ions near the equatorial plane, consistent with the theoretical framework presented by T. W. Hill (1979).

The average H^+ densities show good agreement with the results from both Thomsen et al. (2010) and Wilson et al. (2017), although Wilson et al. (2017) density values are slightly higher than ours between 5 and 11 R_S. H_2^+

21699402, 2026, 4, Downloaded from https://agupubs.onlinelibrary.wiley.com/doi/10.1029/2025JA034738 by Los Alamos National Laboratory, Wiley Online Library on [30/07/2026]. See the Terms and Conditions (https://onlinelibrary.wiley.com/terms-and-conditions) on Wiley Online Library for rules of use; OA articles are governed by the applicable Creative Commons License

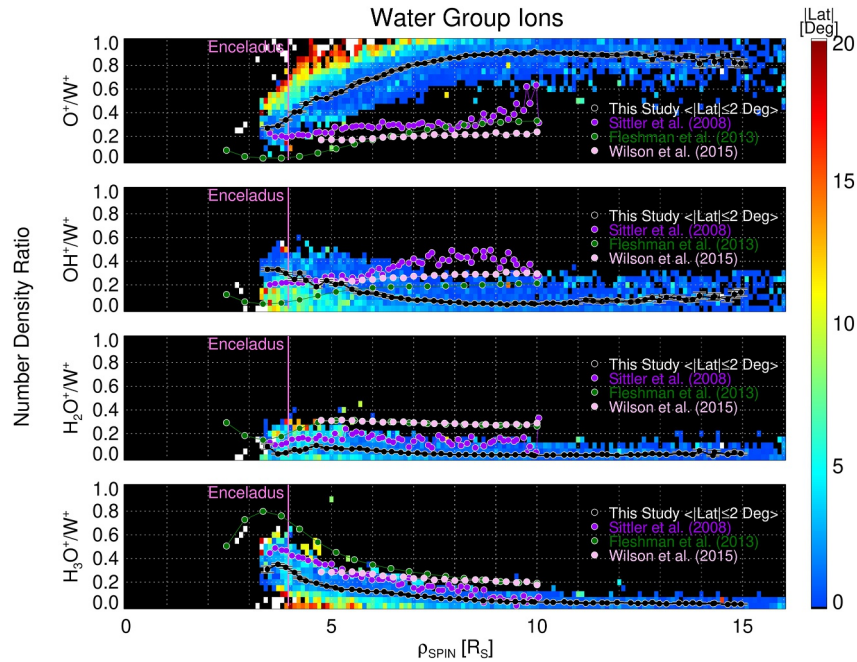


Figure 12. From top to bottom, the panels show number density ratios of O^+/W^+, OH^+/W^+, H_2O^+/W^+, and H_3O^+/W^+ is shown where W^+ is the sum of O^+, OH^+, H_2O^+, and H_3O^+. In each panel, average density ratio values within ±2° latitude of the centrifugal plane from this study are shown with black dots. The color scale represents the average of the absolute latitude values. For comparison, density ratio values from Sittler Jr et al. (2008) are shown with purple dots, Fleshman et al. (2013) model in green dots, and Wilson et al. (2015) with magenta dots.

densities also align with Thomsen et al. (2010), though our radial trend is notably flatter. N^+ densities are significantly higher than those of H^+ and H_2^+, but they decrease more rapidly with increasing radial distance.

W^+ densities agree with Thomsen et al. (2010) up to ~9 R_S, beyond which our values are substantially higher. Wilson et al. (2017) showed similar trends but consistently lower densities overall. Part of the reason for the significantly low W^+ densities in Thomsen et al. (2010) was an unfortunate typo in the code used to derive moments (as discussed in Wilson et al., 2021). Notably, the same erroneous code was also employed in Waite and Furman (2022).

It is crucial to emphasize that neither Thomsen et al. (2010) nor Wilson et al. (2017) derived number densities for individual water group ions. Their analyses used SNG data, which lacks mass-resolving capability; although Thomsen et al. (2010) incorporated TOF-ST data, it was used only to estimate relative ion fractions based on preliminary TOF curves. Both studies assumed a representative mass and treated the entire water group as a single species (W^+), which likely introduces errors due to ion-specific differences in CAPS-IMS detection efficiencies (see Smith et al., 2019). Furthermore, their analyses likely included N^+ in the W^+ population, as they lacked the capabilities to distinguish individual ion signals, introducing additional uncertainty. Our results clearly show that W^+ ions are the dominant species, with a peak density near ~4.5 R_S.

4.3. Water Group Ion Composition (O^+, OH^+, H_2O^+, and H_3O^+)

Figure 12 shows the number density ratios of water group ions, where each ion's number density is normalized by the total water group ion density. To date, water group ion composition (i.e., number density ratio) has been studied by Sittler Jr et al. (2008), Fleshman et al. (2013), and Wilson et al. (2015). Both Sittler Jr et al. (2008) and Wilson et al. (2015) attempted to extract ion number densities directly from the CAPS-IMS TOF-ST data using preliminary TOF curves, while the results from Fleshman et al. (2013) are based on a physical chemistry model constrained by preliminary data from CAPS, RPWS, and INMS.

21699402, 2026, 4, Downloaded from https://agupubs.onlinelibrary.wiley.com/doi/10.1029/2025JA034738 by Los Alamos National Laboratory, Wiley Online Library on [30/07/2026]. See the Terms and Conditions (https://onlinelibrary.wiley.com/terms-and-conditions) on Wiley Online Library for rules of use; OA articles are governed by the applicable Creative Commons License

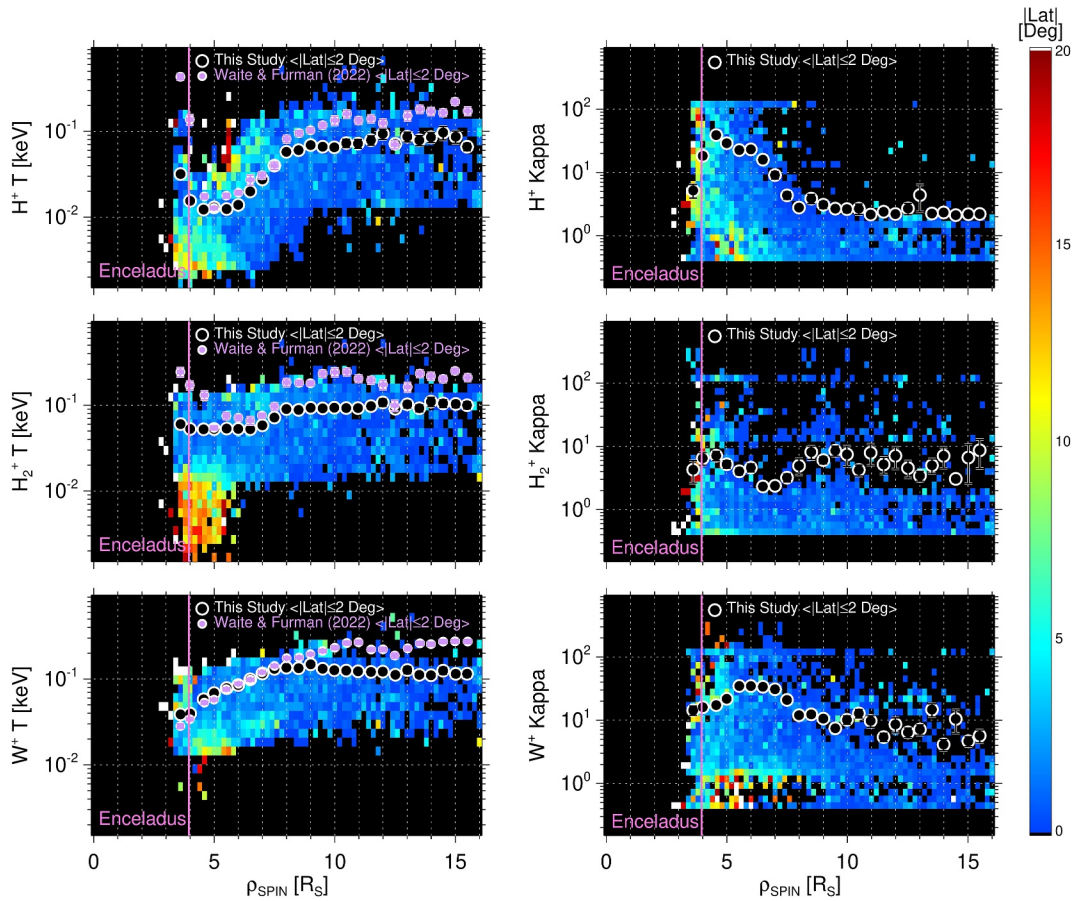


Figure 13. Temperatures and kappa values for H^+, H_2^+, and W^+. Black dots indicate the average temperature values from this study within ±2° latitude of the equatorial plane. The color scale represents the average of the absolute latitude values. Error bars represent the standard deviation of the mean and are generally comparable to or smaller than the symbol size. Temperatures from Waite and Furman (2022) are shown with magenta dots.

As shown in Figure 12, none of these previous studies match our results. Our results indicate that O^+ dominates the water group composition beyond ~8 R_S, comprising over 80% of W^+ in that region. Closer to Enceladus (~3.95 R_S), molecular ions such as OH^+ and H_3O^+ dominate, with their peak densities occurring inside Enceladus' orbital distance. Given that OH^+, H_2O^+, and H_3O^+ decrease with radial distance while O^+ increases, it suggests that molecular ions undergo dissociation and ionization into O^+ at higher rates than previously thought.

Beyond ~9 R_S, the water group ion composition appears nearly frozen, implying a lack of significant sources of O^+, OH^+, H_2O^+, and H_3O^+, as well as the absence of neutral species that could contribute to their production through physical and chemical interactions. While there may be additional sources of O^+ from moons such as Rhea and Dione (which are known as a source of O_2^+, Martens et al., 2008; Teolis & Waite, 2016; Tokar et al., 2012), their contributions are not as substantial as that of Enceladus. Moreover, to meaningfully alter the ion composition beyond 9 R_S, any source would have to be a significant amount, given the rapid increase in spatial volume with radial distance. This volumetric expansion dilutes number densities, thereby influencing the calculated composition in terms of number density ratios.

4.4. Temperature and Thermodynamic Kappa

Figure 13 shows the derived temperatures and kappa values for H^+, H_2^+, and W^+ ions. The purple dots indicate the average temperatures reported by Waite and Furman (2022) within ±2° latitude of the equatorial plane. All ion temperatures increase rapidly out to 8 R_S, beyond which they level off and remain approximately constant.

21699402, 2026, 4, Downloaded from https://agupubs.onlinelibrary.wiley.com/doi/10.1029/2025JA034738 by Los Alamos National Laboratory, Wiley Online Library on [30/07/2026]. See the Terms and Conditions (https://onlinelibrary.wiley.com/terms-and-conditions) on Wiley Online Library for rules of use; OA articles are governed by the applicable Creative Commons License

21699402, 2026, 4, Downloaded from https://agupubs.onlinelibrary.wiley.com/doi/10.1029/2025JA034738 by Los Alamos National Laboratory, Wiley Online Library on [30/07/2026]. See the Terms and Conditions (https://onlinelibrary.wiley.com/terms-and-conditions) on Wiley Online Library for rules of use; OA articles are governed by the applicable Creative Commons License

However, the temperatures of H^+ and H_2^+ show a localized decrease between ~3.5 R_S and ~4.5 R_S. The average values from Waite and Furman (2022) show a similar overall trend but are generally higher than our values, particularly beyond 8 R_S for all ion species and inside 5 R_S for H^+ and H_2^+.

Ion temperatures are generally higher near the equatorial plane for all ion species, with the exception of H^+ between 5 and 8 R_S, where a hotter population is observed at higher latitudes. This region also corresponds to where H^+ temperatures rise most steeply.

The kappa values for H^+ show an inverse trend relative to the H^+ temperatures. Specifically, H^+ kappa values increase sharply from 3.5 R_S to 4.5 R_S and then remain relatively stable out to ~7 R_S, beyond which they drop dramatically. The region between ~5 R_S and ~7 R_S shows high kappa values (also evident in Figure 8), possibly indicating a state of near Maxwell-Boltzmann equilibrium (Livadiotis & McComas, 2011, 2013; Pierrard & Lazar, 2010), where a Maxwell-Boltzmann approximation (i.e., $\kappa \to \infty$) is a reasonable assumption. However, it is evident that most of the data supports the use of kappa distributions over the Maxwell-Boltzmann distributions, as the latter may yield inaccurate plasma parameters (Nicolaou & Livadiotis, 2016).

The H_2^+ kappa values also rise sharply from ~3.5 R_S to ~4.5 R_S, remain relatively stable out to ~6 R_S, then decrease significantly until ~7 R_S, beyond which they increase again and stabilize beyond ~9 R_S. W^+ kappa increases from ~3.5 R_S to ~6 R_S, remains roughly constant to ~7 R_S, and then shows a general decreasing trend. No clear latitudinal dependence is observed in the kappa values for any of the ion species.

One should note that kappa distribution with $\kappa > 10$ for particles having temperatures less than 1 keV is not significantly different than those from Maxwell-Boltzmann distribution (Nicolaou & Livadiotis, 2016). Thus, the Maxwell-Boltzmann approximation holds well for water group ion species in Saturn's magnetosphere, as shown in Figures 7 and 8.

Figure 14 shows the local time dependence of temperature and kappa within ±2° latitude of the equatorial plane. At larger radial distances, the dawn and midnight sectors of the magnetosphere consistently show higher temperatures for all ion species compared to other local times, whereas the noon sector generally shows lower temperatures. The dusk sector closely follows the local-time-averaged temperature trend beyond ~7 R_S but shows the lowest temperature within ~7 R_S.

The kappa values show pronounced local time dependence, particularly in the dawn and dusk sectors. Notably, kappa for H_2^+ in the dusk sector near Enceladus' orbital distance reaches an exceptionally high value. This behavior is also observed in the total ion number density and flow speed (shown in Figures 9 and 10), indicating a clear relationship among these parameters.

5. Discussion

Figure 15 shows the equatorial ion composition (i.e., number density ratios) within ±2° latitude of the equatorial plane, together with the orbital distances of Enceladus, Tethys, Dione, and Rhea. Beyond Enceladus, O^+ becomes the dominant ion species while H_3O^+ and OH^+ dominate inside its orbit. Since Enceladus is the only plausible significant source of O^+, this distribution suggests that O^+ primarily originates from the dissociation and ionization of molecular ions such as H_3O^+ and OH^+.

A sharp increase in the O^+ fraction is observed between ~5 and ~7 R_S, coinciding with the radial region where the plasma flow speed increases rapidly (Figure 9). The dissociation of molecular ions in this region leads to a net increase in ion production in the equatorial plasma sheet. Assuming that the height-integrated Pedersen conductivity at Saturn's ionosphere does not vary strongly across these L-shells, the enhanced ion production strengthens magnetosphere-ionosphere coupling and accelerates the plasma toward rigid corotation (T. W. Hill, 1979). The concurrent increase in H^+ fraction beyond Enceladus' orbital distance further supports the interpretation that atomic ions are efficiently produced through the molecular dissociation and ionization of Enceladus-sourced neutrals.

The strong radial gradients in ion density and flow speed identified in this study within ~5–7 R_S are qualitatively consistent with earlier RPWS-based analyses. Holmberg et al. (2012) reported enhanced ion densities and increasing ion drift velocities within Saturn's inner plasma torus, particularly near Enceladus' orbital distance,

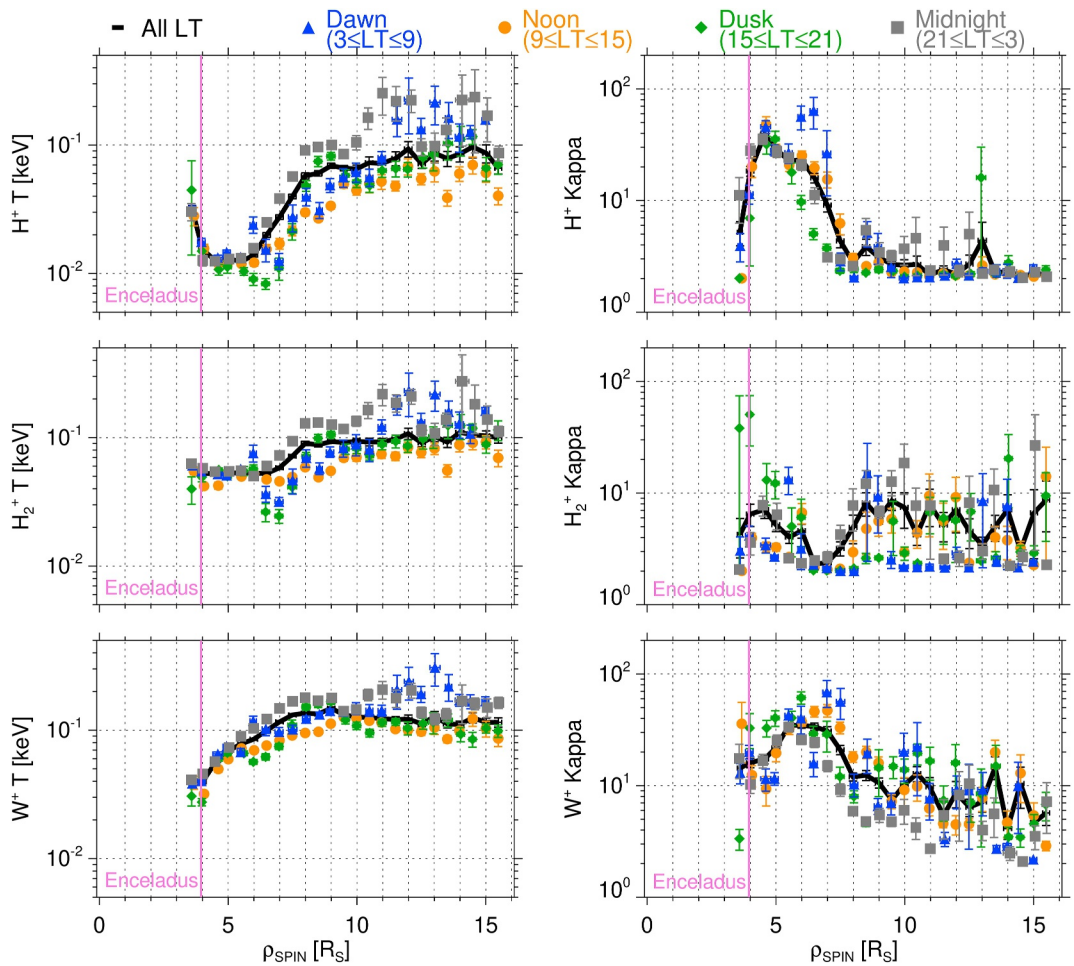


Figure 14. Radial profiles of temperature and kappa for H^+, H_2^+, and W^+ ions within ±2° latitude of the equatorial plane, shown for different local time sectors. Black solid lines represent averages over all local times (and is shown in black dots in Figure 13), while individual local time sectors are indicated by distinct colors and symbols, as annotated at the top of the figure.

using plasma wave observations. Although those results did not resolve individual ion species, the spatial trends inferred from RPWS agree well with the density and flow enhancements derived here from CAPS-IMS forward modeling.

Our results indicate that molecular ions dissociate and ionize into O^+ at higher rates than previously thought. This trend is consistent with the composition profiles reported by H. T. Smith and Richardson (2021). The primary neutral source, H_2O vented from Enceladus, undergoes rapid collisional interactions and charge exchange to form a dense neutral torus near the Enceladus' orbit. This water is only weakly ionized by hot electrons but is efficiently dissociated by photodissociation into OH and O, producing extended neutral tori. In the low-flow region close to Enceladus, H_3O^+ forms through charge-exchange processes, but it tends to recombine quickly back into H_2O. As a result, the dominant region of plasma mass loading is shifted outward, peaking between ∼6 and ∼9 R_S.

The OH torus is further dispersed through dipole-dipole interactions between neutral molecules (Cassidy & Johnson, 2010; Farmer, 2009), as well as through dissociation and charge exchange. Finally, the O torus is greatly expanded throughout the entire magnetosphere through charge-exchange. The latitudinal trend further supports this interpretation. The O^+/W^+ density ratio increases with latitude, whereas the molecular ion fractions generally decrease with latitude (with little variation observed in H_2O^+). This pattern is observed out to ∼8 R_S. The preferential confinement of the heavier W^+ population near the equator, stronger than that of O^+ alone, suggests

21699402, 2026, 4, Downloaded from https://agupubs.onlinelibrary.wiley.com/doi/10.1029/2025JA034738 by Los Alamos National Laboratory, Wiley Online Library on [30/07/2026]. See the Terms and Conditions (https://onlinelibrary.wiley.com/terms-and-conditions) on Wiley Online Library for rules of use; OA articles are governed by the applicable Creative Commons License

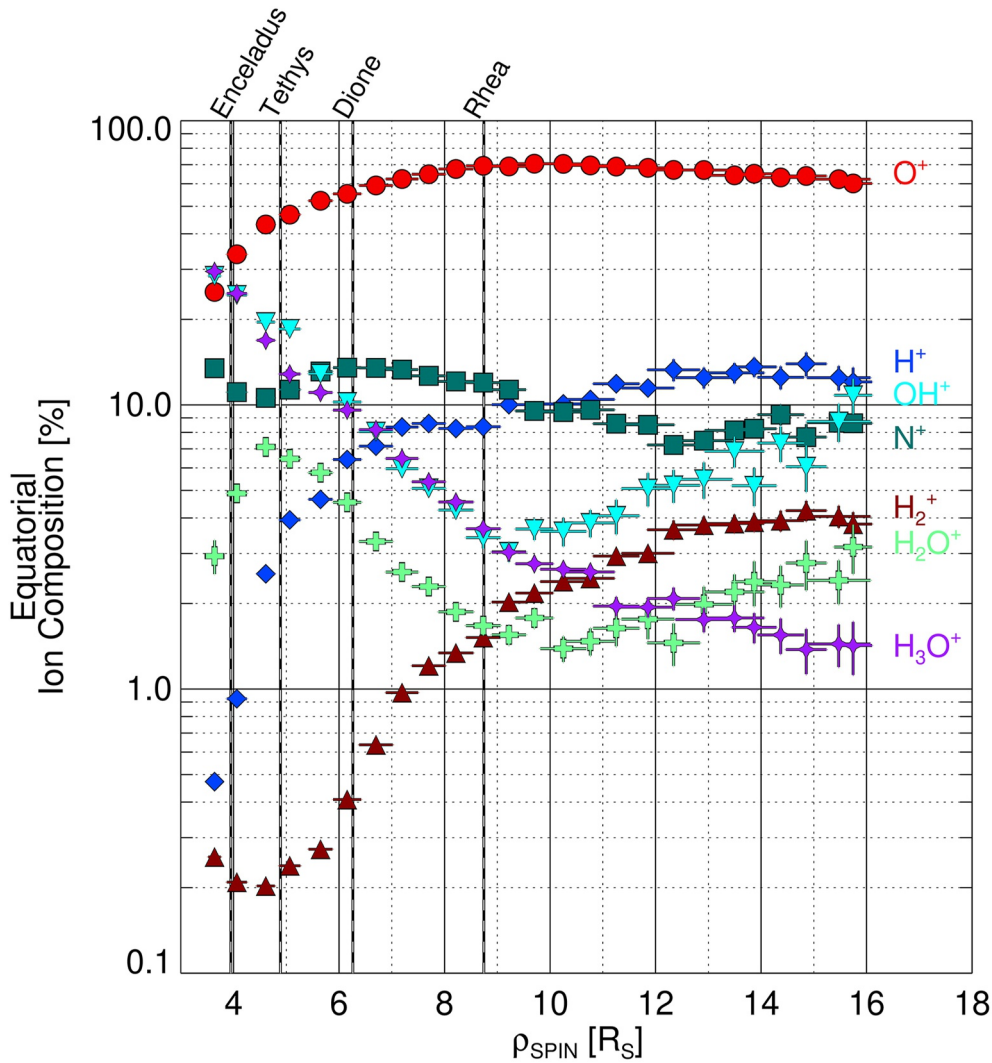


Figure 15. Ion composition (i.e., ion number density ratio in percentage) of Saturnian magnetospheric ions H^+, H_2^+, N^+, O^+, OH^+, H_2O^+, and H_3O^+ within ±2° latitude of the equatorial plane. Locations of four moons (Enceladus, Tethys, Dione, and Rhea) are highlighted.

that centrifugal confinement is more effective on the total water group ion population, likely due to its greater average mass.

The thermodynamic kappa provides additional insight in to the plasma state in this region. Both H^+ and W^+ kappa peak between ~5 and ~7 R_S, coinciding with the rapid increases in O^+ fraction and flow speed. Previous CAPS observations also showed that the flux tube content peaks in this same region (Chen et al., 2010; Sittler Jr et al., 2008), consistent with enhanced ionization rates where electron density and temperature are optimally matched to ionization cross sections (H. T. Smith et al., 2018). Because this radial zone corresponds to the region of highest ion production, Coulomb collisions are likely to play an increasingly important role in shaping the plasma distribution. Taken together, these results suggest that the Saturnian plasma approaches a Maxwell-Boltzmann equilibrium in this region, reflecting a locally enhanced degree of collisional thermalization.

The N^+ fraction peaks inside Enceladus' orbit, decreases near Tethys' orbital distance, and shows a secondary peak near Dione's orbit, remaining relatively constant out to Rhea's orbit. Interestingly, the H_2O^+ fraction peaks near Tethys' orbit rather than at Enceladus' orbit. In contrast, H_2^+ shows a minimum near Tethys and generally shows an anti-correlation with the radial profile of H_2O^+ out to Rhea's orbit. This strong anti-correlation suggests

21699402, 2026, 4, Downloaded from https://agupubs.onlinelibrary.wiley.com/doi/10.1029/2025JA034738 by Los Alamos National Laboratory, Wiley Online Library on [30/07/2026]. See the Terms and Conditions (https://onlinelibrary.wiley.com/terms-and-conditions) on Wiley Online Library for rules of use; OA articles are governed by the applicable Creative Commons License

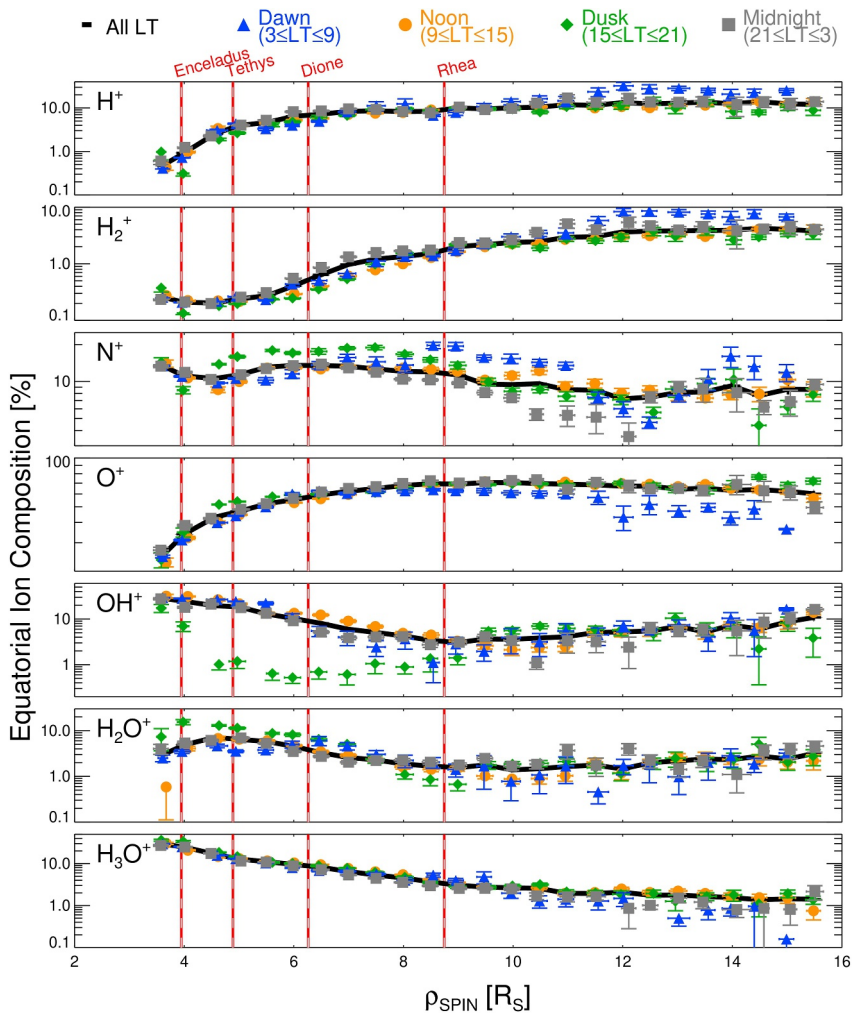


Figure 16. Equatorial ion composition is shown in Figure 15 but with comparison in different local times. The *y*-axis range of each panel is zoomed-in for maximal visibility of the differences.

that H_2^+ and H_2O^+ are closely linked through physical chemistry interactions. While Tethys and Dione have been proposed as potential ion sources (Burch et al., 2007; Frank et al., 1980; Wahlund et al., 2005), it remains unclear whether they provide neutral sources that contribute to the formation of N^+ and H_2O^+. Our analysis clearly shows a distinct peak of N^+ near Dione and H_2O^+ near Tethys, in addition to the O_2^+ detection near Dione (Tokar et al., 2012).

While Figure 15 highlights the radial evolution of equatorial ion composition, Figure 16 further examines these results by separating the equatorial ion composition into different local time sectors. The dusk sector shows the largest variation from the local time-averaged trend. Near Enceladus' orbital distance, H^+, H_2^+, N^+, OH^+ show significant decreases, whereas H_2O^+ shows an increase in abundance. At this radial distance, the overall ion number density in the dusk sector increased by nearly an order of magnitude (Figure 10), and the flow speed increased by nearly 20% relative to the average value (Figure 9). The enhanced ion number density likely strengthens the electromagnetic coupling between the equatorial plasma sheet and Saturn's ionosphere, leading to a more efficient transfer of planetary rotational energy into azimuthal plasma acceleration (T. W. Hill, 1979).

Apparent local time asymmetries in ion density and flow speed have also been reported in earlier RPWS-based studies. M. Holmberg et al. (2014) identified systematic dayside–nightside differences in ion densities and velocities within ~4–6 R_S, attributing these asymmetries to magnetosphere–ionosphere coupling and variations in

21699402, 2026, 4, Downloaded from https://agupubs.onlinelibrary.wiley.com/doi/10.1029/2025JA034738 by Los Alamos National Laboratory, Wiley Online Library on [30/07/2026]. See the Terms and Conditions (https://onlinelibrary.wiley.com/terms-and-conditions) on Wiley Online Library for rules of use; OA articles are governed by the applicable Creative Commons License

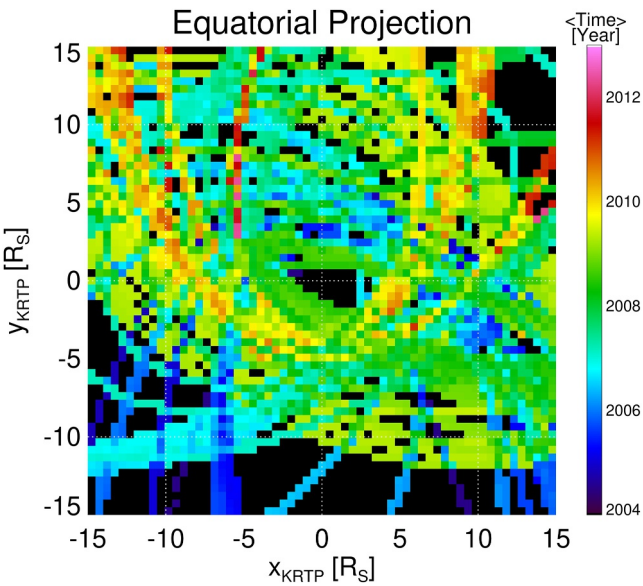


Figure 17. Equatorial projection of the average CAPS observation time (years) for data within 15 R_S. Sampling of the dusk sector occurred predominantly during the early phase (2005–2007) of the Cassini mission.

plasma production. While our CAPS-based results extend to larger radial distances and resolve individual ion species, the qualitative local time trends identified here are consistent with those earlier findings. Modeling work further supports this interpretation: Sakai et al. (2013) demonstrated that dust–plasma interactions and magnetosphere–ionosphere coupling can significantly modify plasma densities and flow patterns in Saturn's plasma sheet.

However, the apparent local time asymmetries shown in Figure 16 must be interpreted with caution. Figure 17 shows the equatorial projection of the average CAPS observation time within 15 R_S, revealing strong temporal sampling biases. Observations in the dusk sector were obtained predominantly during the early phase of the Cassini mission (2005–2007), whereas dawn-sector observations were acquired mainly during later mission phases. Previous studies have shown that ion densities in Saturn's magnetosphere were systematically higher during the early mission interval compared to the later phases (Christon et al., 2013; Elrod et al., 2014; Tseng et al., 2013), reflecting seasonal variations in solar illumination and neutral source strength. Consequently, the observed local time variations primarily reflect temporal and seasonal sampling effects rather than persistent intrinsic local time structure.

The apparent dawn-sector enhancement of OH^+ is likely explained by its broader spatial distribution compared to H_2O^+ and H_3O^+, combined with the temporal sampling bias. Because OH^+ is more radially and latitudinally extended, it remains detectable during later mission phases when overall plasma densities were lower, creating the appearance of a dawn-sector enhancement. Thus, the observed local time patterns reflect the combined effects of spatial ion distributions and temporal evolution of Saturn's magnetosphere.

6. Summary

We derived the individual properties of O^+, OH^+, H_2O^+, and H_3O^+ (i.e., water group ions) by forward modeling CAPS-IMS TOF-ST spectra obtained between mid-2004 to mid-2012, using the TOF response functions based on H. Smith et al. (2019). Our analysis spans radial distances from 4 to 16 R_S. The results confirm that water group ions, particularly O^+, constitute the majority of Saturn's magnetospheric ion population. Tables 1–3 provide a quantitative overview of the derived plasma properties for H^+, H_2^+, N^+, O^+, OH^+, H_2O^+, and H_3O^+. We summarize our findings as follows,

- H_3O^+ and OH^+ dissociate and ionize rapidly and produce large amounts of O^+ between ∼5 and ∼7 R_S. This region coincides where the flow speed increased from ∼40% to 70% with respect to rigid corotation speed.
- All Saturnian magnetospheric ions, except H_2^+, approach Maxwell-Boltzmann equilibrium between ∼5 and ∼7 R_S (indicated by high kappa values). Beyond 7 R_S, all ion distributions become increasingly non-Maxwellian with lower kappa values, reflecting enhanced suprathermal tails.
- O^+ is the dominant ion species in Saturn's magnetosphere comprising up to ∼70% of all magnetospheric ions.
- Beyond, ∼10 R_S, magnetospheric ions are largely composed of O^+ and H^+, indicating that molecular ions generated in the inner magnetosphere of Saturn become completely dissociated into atomic ion species.
- Apparent local time asymmetries in ion density and composition are shown to arise primarily from temporal and seasonal sampling effects during the Cassini mission, rather than from persistent intrinsic local time structure.

21699402, 2026, 4, Downloaded from https://agupubs.onlinelibrary.wiley.com/doi/10.1029/2025JA034738 by Los Alamos National Laboratory, Wiley Online Library on [30/07/2026]. See the Terms and Conditions (https://onlinelibrary.wiley.com/terms-and-conditions) on Wiley Online Library for rules of use; OA articles are governed by the applicable Creative Commons License

Table 1
Summary of 1-D Flow Speed, Total Ion Density, and Individual Ion Densities for H^+, H_2^+, N^+, O^+, OH^+, H_2O^+, and H_3O^+ Within ±2° Latitude of the Equatorial Plane

ρ_{SPIN} [R_S]	V_F [km/s]	n(Total) [cm^{-3}]	n(H^+) [cm^{-3}]	n(H_2^+) [cm^{-3}]	n(N^+) [cm^{-3}]	n(O^+) [cm^{-3}]	n(OH^+) [cm^{-3}]	n(H_2O^+) [cm^{-3}]	n(H_3O^+) [cm^{-3}]
3.5	13.96 (13.81)	47.04 (32.14)	0.31 (0.16)	0.09 (0.08)	5.73 (4.14)	14.96 (8.64)	10.40 (7.78)	3.23 (0.06)	12.34 (8.61)
	±0.28	±2.97	±0.06	±0.00	±0.40	±1.37	±0.43	±0.49	±0.72
4.5	18.08 (17.92)	60.52 (39.85)	1.12 (0.89)	0.11 (0.08)	6.85 (4.36)	26.58 (17.04)	10.75 (7.09)	5.03 (2.20)	10.08 (6.65)
	±0.24	±2.51	±0.04	±0.00	±0.36	±1.23	±0.48	±0.35	±0.44
5.5	28.81 (29.92)	49.80 (29.02)	1.77 (1.21)	0.13 (0.07)	6.95 (3.54)	26.40 (14.59)	5.51 (2.79)	3.51 (1.33)	5.54 (3.28)
	±0.31	±1.69	±0.05	±0.00	±0.28	±0.94	±0.24	±0.19	±0.21
6.5	40.92 (41.45)	30.23 (15.66)	1.69 (0.98)	0.15 (0.08)	4.50 (2.09)	17.55 (8.88)	2.24 (0.80)	1.49 (0.42)	2.61 (1.42)
	±0.33	±1.20	±0.06	±0.01	±0.22	±0.69	±0.13	±0.10	±0.12
7.5	54.03 (54.54)	15.93 (8.48)	1.18 (0.59)	0.16 (0.08)	2.32 (1.01)	9.93 (5.47)	0.91 (0.19)	0.48 (0.11)	0.95 (0.49)
	±0.31	±0.77	±0.06	±0.01	±0.15	±0.46	±0.06	±0.04	±0.05
8.5	63.96 (64.18)	7.60 (4.60)	0.60 (0.34)	0.11 (0.06)	1.03 (0.48)	5.01 (3.14)	0.36 (0.03)	0.16 (0.03)	0.33 (0.17)
	±0.30	±0.34	±0.03	±0.01	±0.06	±0.21	±0.03	±0.01	±0.02
9.5	68.80 (68.67)	5.17 (2.89)	0.43 (0.24)	0.09 (0.05)	0.62 (0.26)	3.42 (2.09)	0.24 (0.02)	0.13 (0.01)	0.23 (0.08)
	±0.33	±0.39	±0.02	±0.00	±0.06	±0.21	±0.02	±0.04	±0.06
10.5	76.41 (76.38)	3.94 (2.45)	0.37 (0.20)	0.09 (0.05)	0.45 (0.19)	2.64 (1.73)	0.20 (0.01)	0.06 (0.01)	0.12 (0.05)
	±0.52	±0.27	±0.03	±0.01	±0.05	±0.17	±0.03	±0.01	±0.01
11.5	82.56 (82.22)	3.30 (2.31)	0.33 (0.22)	0.09 (0.07)	0.29 (0.15)	2.24 (1.50)	0.21 (0.04)	0.07 (0.01)	0.08 (0.04)
	±0.92	±0.27	±0.02	±0.01	±0.03	±0.19	±0.03	±0.01	±0.01
12.5	88.88 (87.28)	2.89 (2.00)	0.29 (0.18)	0.09 (0.07)	0.25 (0.13)	1.92 (1.27)	0.21 (0.03)	0.06 (0.01)	0.07 (0.03)
	±1.21	±0.22	±0.02	±0.01	±0.03	±0.15	±0.04	±0.01	±0.01
13.5	99.93 (97.99)	1.98 (1.54)	0.22 (0.16)	0.07 (0.05)	0.18 (0.11)	1.28 (0.91)	0.14 (0.03)	0.06 (0.01)	0.04 (0.02)
	±1.79	±0.13	±0.02	±0.00	±0.01	±0.09	±0.02	±0.01	±0.00
14.5	105.78 (105.99)	1.40 (1.01)	0.16 (0.12)	0.05 (0.04)	0.14 (0.07)	0.89 (0.66)	0.11 (0.05)	0.03 (0.01)	0.02 (0.01)
	±2.42	±0.13	±0.01	±0.00	±0.02	±0.09	±0.02	±0.01	±0.00
15.5	113.34 (111.97)	1.35 (1.05)	0.13 (0.11)	0.04 (0.03)	0.13 (0.08)	0.89 (0.55)	0.10 (0.07)	0.04 (0.02)	0.03 (0.01)
	±2.36	±0.15	±0.01	±0.00	±0.03	±0.11	±0.01	±0.01	±0.01

Note. For each ion species, the average values (with the median given in parenthesis) and the associated standard deviation of the mean (reported to two decimal points) are shown. The averages and medians are computed within ±0.5 R_S bins of the equatorial radial distance ρ_{SPIN}.

21699402, 2026, 4, Downloaded from https://agupubs.onlinelibrary.wiley.com/doi/10.1029/2025JA034738 by Los Alamos National Laboratory, Wiley Online Library on [30/07/2026]. See the Terms and Conditions (https://onlinelibrary.wiley.com/terms-and-conditions) on Wiley Online Library for rules of use; OA articles are governed by the applicable Creative Commons License

Table 2
Summary of Temperature and Kappa Values for H^+, H_2^+, and W^+ Within ±2° Latitude of the Equatorial Plane

ρ_{SPIN} [R_S]	$T(H^+)$ [eV]	$T(H_2^+)$ [eV]	$T(W^+)$ [eV]	$\kappa(H^+)$	$\kappa(H_2^+)$	$\kappa(W^+)$
3.5	24.79 (15.58)	59.46 (57.01)	39.50 (38.48)	8.09 (2.01)	5.33 (2.01)	15.74 (3.45)
	±1.26	±1.17	±0.70	±1.23	±1.57	±1.73
4.5	12.65 (11.09)	51.09 (50.81)	55.83 (55.01)	33.01 (11.29)	6.68 (2.70)	17.47 (6.30)
	±0.26	±0.64	±0.79	±1.62	±0.70	±1.12
5.5	12.75 (11.35)	52.90 (51.57)	77.57 (74.82)	23.29 (8.06)	4.54 (2.10)	32.40 (9.88)
	±0.21	±0.71	±0.92	±1.13	±0.44	±1.41
6.5	19.48 (13.65)	53.36 (47.14)	99.31 (87.56)	16.89 (4.26)	2.63 (2.01)	33.91 (10.51)
	±0.58	±1.00	±1.48	±1.12	±0.18	±1.73
7.5	42.30 (33.35)	74.27 (64.43)	130.02 (126.09)	5.15 (2.23)	2.97 (2.01)	20.51 (6.84)
	±1.58	±1.83	±2.14	±0.57	±0.28	±1.51
8.5	60.07 (46.00)	88.12 (74.86)	136.35 (132.56)	3.21 (2.04)	7.06 (2.12)	11.93 (5.06)
	±2.02	±2.25	±2.42	±0.32	±1.19	±0.83
9.5	69.40 (53.24)	94.49 (82.69)	138.21 (129.68)	2.93 (2.02)	7.82 (2.38)	8.75 (3.91)
	±2.59	±2.50	±2.55	±0.27	±1.18	±0.74
10.5	69.57 (41.06)	92.00 (65.09)	123.59 (108.67)	2.70 (2.01)	5.97 (2.25)	11.76 (3.71)
	±5.11	±4.15	±3.70	±0.33	±1.20	±1.33
11.5	78.31 (50.02)	96.74 (71.92)	119.36 (108.71)	2.30 (2.01)	6.02 (2.25)	7.88 (3.46)
	±6.53	±4.79	±4.46	±0.11	±1.31	±1.32
12.5	84.65 (58.37)	100.27 (82.87)	119.67 (101.38)	3.38 (2.01)	4.79 (2.18)	6.58 (3.30)
	±7.48	±6.50	±5.93	±0.97	±1.20	±0.85
13.5	82.69 (59.20)	101.91 (75.40)	118.92 (101.98)	2.37 (2.01)	5.35 (2.26)	10.16 (3.07)
	±7.82	±7.35	±7.17	±0.15	±1.15	±1.86
14.5	85.18 (71.32)	98.76 (91.18)	116.47 (98.51)	2.22 (2.01)	5.25 (2.29)	7.95 (2.57)
	±9.73	±7.07	±7.41	±0.07	±1.89	±2.21
15.5	77.64 (65.05)	104.39 (97.47)	116.46 (102.59)	2.22 (2.01)	5.61 (2.37)	4.57 (2.95)
	±8.96	±7.82	±6.56	±0.05	±2.04	±0.68

Note. For each ion species, the average values (with the median given in parenthesis) and the associated standard deviation of the mean (reported to two decimal points) are shown. The averages and medians are computed within ±0.5 R_S bins of the equatorial radial distance ρ_{SPIN}.

21699402, 2026, 4, Downloaded from https://agupubs.onlinelibrary.wiley.com/doi/10.1029/2025JA034738 by Los Alamos National Laboratory, Wiley Online Library on [30/07/2026]. See the Terms and Conditions (https://onlinelibrary.wiley.com/terms-and-conditions) on Wiley Online Library for rules of use; OA articles are governed by the applicable Creative Commons License

21699402, 2026, 4, Downloaded from https://agupubs.onlinelibrary.wiley.com/doi/10.1029/2025JA034738 by Los Alamos National Laboratory, Wiley Online Library on [30/07/2026]. See the Terms and Conditions (https://onlinelibrary.wiley.com/terms-and-conditions) on Wiley Online Library for rules of use; OA articles are governed by the applicable Creative Commons License

Table 3
Summary of Ion Composition, Expressed as Number Density Ratios (%) for H^+, H_2^+, N^+, O^+, OH^+, H_2O^+, and H_3O^+, Within ±2° Latitude of the Equatorial Plane

ρ_{SPIN} [R_S]	H^+ [%]	H_2^+ [%]	N^+ [%]	O^+ [%]	OH^+ [%]	H_2O^+ [%]	H_3O^+ [%]
3.5	0.60 (0.48) ±0.03	0.24 (0.22) ±0.01	12.67 (12.86) ±0.64	28.57 (28.24) ±1.44	25.91 (27.23) ±1.31	3.57 (0.30) ±0.18	28.44 (27.87) ±1.43
4.5	2.53 (1.97) ±0.09	0.21 (0.19) ±0.01	10.72 (10.69) ±0.38	42.08 (41.74) ±1.50	20.72 (23.46) ±0.74	6.58 (5.83) ±0.23	17.16 (15.86) ±0.61
5.5	5.10 (4.11) ±0.16	0.30 (0.25) ±0.01	12.74 (12.52) ±0.39	51.82 (52.30) ±1.58	13.56 (13.63) ±0.41	5.63 (5.26) ±0.17	10.85 (11.03) ±0.33
6.5	7.14 (6.33) ±0.23	0.64 (0.49) ±0.02	13.62 (13.40) ±0.44	58.98 (58.57) ±1.92	7.95 (5.51) ±0.26	3.42 (2.61) ±0.11	8.25 (8.17) ±0.27
7.5	8.53 (7.76) ±0.30	1.20 (0.98) ±0.04	12.62 (12.16) ±0.44	64.91 (64.88) ±2.28	5.13 (2.07) ±0.18	2.23 (1.31) ±0.08	5.37 (5.38) ±0.19
8.5	8.61 (7.81) ±0.32	1.55 (1.41) ±0.06	12.10 (11.34) ±0.45	68.78 (68.97) ±2.54	3.53 (0.58) ±0.13	1.70 (0.56) ±0.06	3.73 (3.76) ±0.14
9.5	9.90 (8.67) ±0.40	2.23 (2.01) ±0.09	9.74 (9.25) ±0.39	70.35 (70.58) ±2.83	3.37 (0.55) ±0.14	1.59 (0.37) ±0.06	2.82 (2.74) ±0.11
10.5	10.67 (9.24) ±0.59	2.52 (2.19) ±0.14	9.50 (8.91) ±0.52	69.67 (70.83) ±3.83	3.74 (0.47) ±0.21	1.51 (0.33) ±0.08	2.39 (2.15) ±0.13
11.5	11.89 (9.93) ±0.89	3.15 (2.74) ±0.24	8.10 (7.29) ±0.61	68.16 (70.62) ±5.09	5.13 (2.10) ±0.38	1.64 (0.48) ±0.12	1.93 (1.84) ±0.14
12.5	12.84 (10.16) ±1.04	3.79 (3.16) ±0.31	7.36 (6.74) ±0.60	66.35 (69.88) ±5.38	5.70 (1.91) ±0.46	2.00 (0.67) ±0.16	1.96 (1.49) ±0.16
13.5	13.44 (12.30) ±1.16	3.93 (3.48) ±0.34	8.46 (7.75) ±0.73	64.29 (68.93) ±5.55	6.06 (2.97) ±0.52	2.21 (0.95) ±0.19	1.62 (1.34) ±0.14
14.5	13.02 (10.90) ±1.47	4.08 (3.56) ±0.46	8.53 (6.96) ±0.96	63.15 (64.71) ±7.10	7.35 (3.95) ±0.83	2.57 (1.05) ±0.29	1.30 (0.71) ±0.15
15.5	12.26 (12.38) ±1.58	3.88 (3.73) ±0.50	8.28 (8.01) ±1.07	62.36 (66.33) ±8.05	8.75 (7.22) ±1.13	2.87 (2.00) ±0.37	1.60 (1.35) ±0.21

Note. For each ion species, the average values (with the median given in parenthesis) and the associated standard deviation of the mean (reported to two decimal points) are shown. The averages and medians are computed within ±0.5 R_S bins of the equatorial radial distance ρ_{SPIN}.

Appendix A: TOF Mass Tracer Derivation and LPP Model Adjustments

A1. Derivation of TOF-ST Mass Tracer Lines

We present newly derived mass tracer lines that represent the peak signal positions of ions in time-of-flight (TOF) spectra. The derivation is based on the CAPS-IMS post-acceleration voltage and the electro-optics configuration of CAPS-IMS ST. The total energy at the carbon foil is defined as

$$E_T[\mathrm{keV}] = ([E_{IN}/Q_{IN}[\mathrm{keV}/e] + 14.557\ [kV] \cdot Q_{IN}[e]), \tag{A1}$$

where E_{IN}/Q_{IN} is the CAPS-IMS energy step in keV/q, and 14.557 kV is the post-acceleration voltage (D. Young et al., 2004). Because Saturn's plasma is dominated by singly charged ions, we adopt $Q_{IN} = 1$. The peak TOF position is then expressed as

$$t_{peak}\ [ns] = \left(\alpha_0 + \alpha_1/\sqrt{E_T\ [\mathrm{keV}]}\right) \cdot M\ [\mathrm{amu}]^{\beta_0+\beta_1 \cdot E_T[\mathrm{keV}]} + (\gamma_0 + \gamma_1 \cdot E_T\ [\mathrm{keV}]), \tag{A2}$$

21699402, 2026, 4, Downloaded from https://agupubs.onlinelibrary.wiley.com/doi/10.1029/2025JA034738 by Los Alamos National Laboratory, Wiley Online Library on [30/07/2026]. See the Terms and Conditions (https://onlinelibrary.wiley.com/terms-and-conditions) on Wiley Online Library for rules of use; OA articles are governed by the applicable Creative Commons License

where M is the ion mass in amu.

For neutralized particles (ions that emerge from the foil as neutrals), the parameters are:

$$\alpha_0 = -17.188,\ \alpha_1 = 513.549,$$

$$\beta_0 = 0.522,\ \beta_1 = 67.763 \cdot 10^{-5},$$

$$\gamma_0 = -3.388,\ \gamma_1 = -0.037.$$

For negative particles (ions that emerge from the foil as negative ions), the parameters are:

$$\alpha_0 = -56.323,\ \alpha_1 = 604.563,$$

$$\beta_0 = 0.335,\ \beta_1 = 810.520 \cdot 10^{-5},$$

$$\gamma_0 = 24.609,\ \gamma_1 = -0.027.$$

These parameterizations were obtained from CAPS-IMS observations where H^+, N^+, O^+, and $O_2{}^+$ peaks were clearly identified. They are used to correct the peak positions of the modified logistic power peak (LPP) functions described in the following section.

A2. Modification to the Logistic Power Peak (LPP) Function

H. Smith et al. (2019) introduced the LPP function to characterize TOF curves for individual ion species. Although these functions were originally developed using TOF curves obtained during flight calibrations, they were not optimized for in situ measurements. In practice, the TOF shapes observed in Saturn's magnetosphere often differ from those measured during calibrations, since variations in operating voltages can modify the instrument's electro-optics and thereby alter the TOF curve shapes. To address this discrepancy, we introduce modifications to the LPP functions that provide better agreement with the in situ data.

For H^+ and $H_2{}^+$, the LPP function fails to reproduce the observed distributions, even after modification. For these ions, we instead adopt a Gaussian-like distribution function,

$$\mathrm{TOF}\,(E,t) = \frac{1}{A_0} \cdot e^{-\frac{(t-t_{\mathrm{peak}})^2}{32}},$$

where A_0 is a normalization constant equal to the integrated TOF distribution at the given energy step, and t_{peak} is the corrected peak position derived earlier.

For all other ion species (i.e., N^+, O^+, OH^+, H_2O^+, and H_3O^+), we retain the original LPP form and parameters from H. Smith et al. (2019), but correct the TOF peak position using the t_{peak} $[ns]$, while also increasing the width parameter by 1.8 and reducing the skewness by 0.5 to better reproduce the in situ TOF curves.

Conflict of Interest

The authors declare no conflicts of interest relevant to this study.

Availability Statement

The CAPS-IMS data products used in this study are publicly available from NASA's PDS archive (CO-E/J/S/SW-CAPS-2-UNCALIBRATED-V1.0, D. T. Young et al., 2013). The forward model results presented in this study have been deposited in the NASA Planetary Data System (Kim, 2024).

Acknowledgments
This work was supported by the NASA Cassini Data Analysis Program (Grant: 80NSSC21K0530).

References

Bagenal, F., & Delamere, P. A. (2011). Flow of mass and energy in the magnetospheres of Jupiter and Saturn. *Journal of Geophysical Research*, *116*(A5), A05209. https://doi.org/10.1029/2010ja016294

Bagnasco, G., Kolm, M., Ferruit, P., Honnen, K., Koehler, J., Lemke, R., et al. (2007). Overview of the near-infrared spectrograph (NIRSpec) instrument on-board the James Webb Space Telescope (JWST). *6692*, 174–187.

Bridge, H., Bagenal, F., Belcher, J., Lazarus, A., McNutt, R., Sullivan, J., et al. (1982). Plasma observations near Saturn: Initial results from Voyager 2. *Science*, *215*(4532), 563–570. https://doi.org/10.1126/science.215.4532.563

Bridge, H., Belcher, J., Butler, R., Lazarus, A., Mavretic, A., Sullivan, J. D., et al. (1977). The plasma experiment on the 1977 Voyager mission. *Space Science Reviews*, *21*(3), 259–287. https://doi.org/10.1007/bf00211542

Bridge, H., Belcher, J., Lazarus, A., Olbert, S., Sullivan, J., Bagenal, F., et al. (1981). Plasma observations near Saturn: Initial results from Voyager 1. *Science*, *212*(4491), 217–224. https://doi.org/10.1126/science.212.4491.217

Brown, R. H., Clark, R. N., Buratti, B. J., Cruikshank, D. P., Barnes, J. W., Mastrapa, R. M., et al. (2006). Composition and physical properties of Enceladus' surface. *Science*, *311*(5766), 1425–1428. https://doi.org/10.1126/science.1121031

Burch, J., Goldstein, J., Lewis, W., Young, D., Coates, A., Dougherty, M., & André, N. (2007). Tethys and Dione as sources of outward-flowing plasma in Saturn's magnetosphere. *Nature*, *447*(7146), 833–835. https://doi.org/10.1038/nature05906

Cassidy, T., & Johnson, R. (2010). Collisional spreading of Enceladus' neutral cloud. *Icarus*, *209*(2), 696–703. https://doi.org/10.1016/j.icarus.2010.04.010

Chen, Y., Hill, T., Rymer, A., & Wilson, R. (2010). Rate of radial transport of plasma in Saturn's inner magnetosphere. *Journal of Geophysical Research*, *115*(A10), A10211. https://doi.org/10.1029/2010ja015412

Christon, S., Hamilton, D., DiFabio, R., Mitchell, D., Krimigis, S., & Jontof-Hutter, D. (2013). Saturn suprathermal O2+ and mass-28+ molecular ions: Long-term seasonal and solar variation. *Journal of Geophysical Research: Space Physics*, *118*(6), 3446–3463. https://doi.org/10.1002/jgra.50383

Dougherty, M., Khurana, K., Neubauer, F., Russell, C., Saur, J., Leisner, J., & Burton, M. (2006). Identification of a dynamic atmosphere at Enceladus with the Cassini magnetometer. *Science*, *311*(5766), 1406–1409. https://doi.org/10.1126/science.1120985

Elrod, M. K., Tseng, W.-L., Woodson, A. K., & Johnson, R. E. (2014). Seasonal and radial trends in Saturn's thermal plasma between the main rings and Enceladus. *Icarus*, *242*, 130–137. https://doi.org/10.1016/j.icarus.2014.07.020

Farmer, A. J. (2009). Saturn in hot water: Viscous evolution of the Enceladus torus. *Icarus*, *202*(1), 280–286. https://doi.org/10.1016/j.icarus.2009.02.031

Felici, M. (2016). Cassini observations of ionospheric plasma sources and plasma distribution in Saturn's magnetosphere. Doctoral Thesis. Retrieved from https://discovery.ucl.ac.uk/id/eprint/1530897

Felici, M., Arridge, C., Wilson, R., Coates, A., Thomsen, M., & Reisenfeld, D. (2018). Survey of thermal plasma composition in Saturn's magnetosphere using time-of-flight data from Cassini/CAPS. *Journal of Geophysical Research: Space Physics*, *123*(8), 6494–6513. https://doi.org/10.1029/2017ja025085

Fleshman, B., Delamere, P., & Bagenal, F. (2010). Modeling the Enceladus plume–plasma interaction. *Geophysical Research Letters*, *37*(3), L03202. https://doi.org/10.1029/2009gl041613

Fleshman, B., Delamere, P., Bagenal, F., & Cassidy, T. (2012). The roles of charge exchange and dissociation in spreading Saturn's neutral clouds. *Journal of Geophysical Research*, *117*(E5), E05007. https://doi.org/10.1029/2011je003996

Fleshman, B., Delamere, P., Bagenal, F., & Cassidy, T. (2013). A 1-D model of physical chemistry in Saturn's inner magnetosphere. *Journal of Geophysical Research: Planets*, *118*(8), 1567–1581. https://doi.org/10.1002/jgre.20106

Frank, L., Burek, B., Ackerson, K., Wolfe, J., & Mihalov, J. (1980). Plasmas in Saturn's magnetosphere. *Journal of Geophysical Research*, *85*(A11), 5695–5708. https://doi.org/10.1029/ja085ia11p05695

Funsten, H. O., Barraclough, B. L., & McComas, D. J. (1994). Interactions of slow H, H2, and H3 with thin carbon foils. *Nuclear Instruments and Methods in Physics Research Section B: Beam Interactions with Materials and Atoms*, *90*(1–4), 24–28. https://doi.org/10.1016/0168-583x(94)95503-4

Gardner, J. P., Mather, J. C., Clampin, M., Doyon, R., Greenhouse, M. A., Hammel, H. B., et al. (2006). The James Webb space telescope. *Space Science Reviews*, *123*, 485–606.

Gombosi, T. I., Armstrong, T. P., Arridge, C. S., Khurana, K. K., Krimigis, S. M., Krupp, N., et al. (2009). Saturn's magnetospheric configuration. *Saturn from Cassini-Huygens*, 203–255.

Gurnett, D. A., Kurth, W. S., Kirchner, D., Hospodarsky, G., Averkamp, T., Zarka, P., et al. (2004). The Cassini radio and plasma wave investigation. *Space Science Reviews*, *114*(1), 395–463. https://doi.org/10.1007/s11214-004-1434-0

Hall, C. F. (1974). Pioneer 10. *Science*, *183*(4122), 301–302. https://doi.org/10.1126/science.183.4122.301

Hansen, C. J., Esposito, L., Stewart, A., Colwell, J., Hendrix, A., Pryor, W., et al. (2006). Enceladus' water vapor plume. *Science*, *311*(5766), 1422–1425. https://doi.org/10.1126/science.1121254

Hill, T., & Michel, F. (1976). Heavy ions from the Galilean satellites and the centrifugal distortion of the Jovian magnetosphere. *Journal of Geophysical Research*, *81*(25), 4561–4565. https://doi.org/10.1029/ja081i025p04561

Hill, T. W. (1979). Inertial limit on corotation. *Journal of Geophysical Research*, *84*(A11), 6554–6558. https://doi.org/10.1029/ja084ia11p06554

Holmberg, M., Wahlund, J., & Morooka, M. (2014). Dayside/nightside asymmetry of ion densities and velocities in Saturn's inner magnetosphere. *Geophysical Research Letters*, *41*(11), 3717–3723. https://doi.org/10.1002/2014gl060229

Holmberg, M. K., Wahlund, J.-E., Morooka, M., & Persoon, A. (2012). Ion densities and velocities in the inner plasma torus of Saturn. *Planetary and Space Science*, *73*(1), 151–160. https://doi.org/10.1016/j.pss.2012.09.016

Jia, Y., Russell, C., Khurana, K., Toth, G., Leisner, J., & Gombosi, T. (2010). Interaction of Saturn's magnetosphere and its moons: 1. Interaction between corotating plasma and standard obstacles. *Journal of Geophysical Research*, *115*(A4), A04214. https://doi.org/10.1029/2009ja014630

Jones, G., Roussos, E., Krupp, N., Paranicas, C., Woch, J., Lagg, A., et al. (2006). Enceladus' varying imprint on the magnetosphere of Saturn. *Science*, *311*(5766), 1412–1415. https://doi.org/10.1126/science.1121011

Kallenbach, R., Gonin, M., Bochsler, P., & Bürgi, A. (1995). Charge exchange of B, C, O, Al, Si, S, F and Cl passing through thin carbon foils at low energies: Formation of negative ions. *Nuclear Instruments and Methods in Physics Research Section B: Beam Interactions with Materials and Atoms*, *103*(2), 111–116. https://doi.org/10.1016/0168-583x(95)00646-x

Kallenbach, R., Gonin, M., Bürgi, A., & Bochsler, P. (1993). Charge exchange of hydrogen ions in carbon foils. *Nuclear Instruments and Methods in Physics Research Section B: Beam Interactions with Materials and Atoms*, *83*(1–2), 68–72. https://doi.org/10.1016/0168-583x(93)95909-o

Kim, T. (2024). Global survey of individual water group ion properties in Saturn's magnetosphere: Cassini CAPS observations [Dataset]. *NASA Planetary Data System*, *97*. https://doi.org/10.17189/wqqj-5z30

21699402, 2026, 4, Downloaded from https://agupubs.onlinelibrary.wiley.com/doi/10.1029/2025JA034738 by Los Alamos National Laboratory, Wiley Online Library on [30/07/2026]. See the Terms and Conditions (https://onlinelibrary.wiley.com/terms-and-conditions) on Wiley Online Library for rules of use; OA articles are governed by the applicable Creative Commons License

Kim, T., Ebert, R., Valek, P., Allegrini, F., McComas, D., Bagenal, F., et al. (2020a). Method to derive ion properties from Juno JADE including abundance estimates for O+ and S2+. *Journal of Geophysical Research: Space Physics*, *125*(2), e2018JA026169. https://doi.org/10.1029/2018ja026169

Kim, T., Ebert, R., Valek, P., Allegrini, F., McComas, D., Bagenal, F., et al. (2020b). Survey of ion properties in Jupiter's plasma sheet: Juno JADE-I observations. *Journal of Geophysical Research: Space Physics*, *125*(4), e2019JA027696. https://doi.org/10.1029/2019ja027696

Kohlhase, C., & Penzo, P. A. (1977). Voyager mission description. *Space Science Reviews*, *21*(2), 77–101. https://doi.org/10.1007/bf00200846

Krimigis, S. M., Mitchell, D. G., Hamilton, D. C., Livi, S., Dandouras, J., Jaskulek, S., et al. (2004). Magnetosphere imaging instrument (MIMI) on the Cassini mission to Saturn/Titan. In *The Cassini-Huygens Mission* (pp. 233–329). Springer.

Livadiotis, G. (2017). *Kappa distributions: Theory and applications in plasmas*. Elsevier.

Livadiotis, G. (2018). Thermodynamic origin of kappa distributions. *EPL (Europhysics Letters)*, *122*(5), 50001. https://doi.org/10.1209/0295-5075/122/50001

Livadiotis, G., & McComas, D. (2011). Invariant kappa distribution in space plasmas out of equilibrium. *The Astrophysical Journal*, *741*(2), 88. https://doi.org/10.1088/0004-637x/741/2/88

Livadiotis, G., & McComas, D. J. (2013). Understanding kappa distributions: A toolbox for space science and astrophysics. *Space Science Reviews*, *175*(1–4), 183–214. https://doi.org/10.1007/s11214-013-9982-9

Livadiotis, G., & McComas, D. J. (2021). Thermodynamic definitions of temperature and kappa and introduction of the entropy defect. *Entropy*, *23*(12), 1683. https://doi.org/10.3390/e23121683

Livadiotis, G., & McComas, D. J. (2023). Entropy defect in thermodynamics. *Scientific Reports*, *13*(1), 9033. https://doi.org/10.1038/s41598-023-36080-w

Livi, R., Goldstein, J., Burch, J., Crary, F., Rymer, A., Mitchell, D., & Persoon, A. (2014). Multi-instrument analysis of plasma parameters in Saturn's equatorial, inner magnetosphere using corrections for corrections for spacecraft potential and penetrating background radiation. *Journal of Geophysical Research: Space Physics*, *119*(5), 3683–3707. https://doi.org/10.1002/2013ja019616

Martens, H. R., Reisenfeld, D. B., Williams, J. D., Johnson, R. E., & Smith, H. T. (2008). Observations of molecular oxygen ions in Saturn's inner magnetosphere. *Geophysical Research Letters*, *35*(20). https://doi.org/10.1029/2008gl035433

Matson, D. L., Spilker, L. J., & Lebreton, J.-P. (2002). The Cassini/Huygens mission to the Saturnian system. *Space Science Reviews*, *104*(1), 1–58. https://doi.org/10.1023/A:1023609211620

Mauk, B., Hamilton, D., Hill, T., Hospodarsky, G., Johnson, R., Paranicas, C., et al. (2009). Fundamental plasma processes in Saturn's magnetosphere. *Saturn from Cassini-Huygens*, 281–331.

McComas, D. J., Nordholt, J. E., Bame, S. J., Barraclough, B. L., & Gosling, J. T. (1990). Linear electric field mass analysis: A technique for three-dimensional high mass resolution space plasma composition measurements. *Proceedings of the National Academy of Sciences of the United States of America*, *87*(15), 5925–5929. https://doi.org/10.1073/pnas.87.15.5925

McKibbin, D., Wolfe, J., Collard, H., Savage, H., & Molari, R. (1977). Plasma analyzer for the Pioneer Jupiter missions. *Space Science Instrumentation*, *3*, 219–228.

Nicolaou, G., & Livadiotis, G. (2016). Misestimation of temperature when applying Maxwellian distributions to space plasmas described by kappa distributions. *Astrophysics and Space Science*, *361*(11), 359. https://doi.org/10.1007/s10509-016-2949-z

Olbert, S. (1968). Summary of experimental results from MIT detector on IMP-1 (pp. 641–659).

Perry, M., Teolis, B., Hurley, D., Magee, B., Waite, J., Brockwell, T., et al. (2015). Cassini INMS measurements of Enceladus plume density. *Icarus*, *257*, 139–162. https://doi.org/10.1016/j.icarus.2015.04.037

Persoon, A., Groene, J., West, E., Kurth, W., Wahlund, J., & Gurnett, D. (2019). Cassini RPWS electron densities from upper hybrid and plasma wave frequencies [Dataset]. *NASA Planetary Data System*. https://doi.org/10.17189/1518302

Pierrard, V., & Lazar, M. (2010). Kappa distributions: Theory and applications in space plasmas. *Solar Physics*, *267*(1), 153–174. https://doi.org/10.1007/s11207-010-9640-2

Porco, C. C., Helfenstein, P., Thomas, P., Ingersoll, A., Wisdom, J., West, R., et al. (2006). Cassini observes the active south pole of Enceladus. *Science*, *311*(5766), 1393–1401. https://doi.org/10.1126/science.1123013

Richardson, J. D. (1986). Thermal ions at Saturn: Plasma parameters and implications. *Journal of Geophysical Research*, *91*(A2), 1381–1389. https://doi.org/10.1029/ja091ia02p01381

Ritzau, S. M., & Baragiola, R. A. (1998). Electron emission from carbon foils induced by keV ions. *Physical Review B*, *58*(5), 2529–2538. https://doi.org/10.1103/physrevb.58.2529

Sakai, S., Watanabe, S., Morooka, M. W., Holmberg, M. K., Wahlund, J.-E., Gurnett, D. A., & Kurth, W. S. (2013). Dust–plasma interaction through magnetosphere–ionosphere coupling in Saturn's plasma disk. *Planetary and Space Science*, *75*, 11–16. https://doi.org/10.1016/j.pss.2012.11.003

Sittler, E., Jr., Andre, N., Blanc, M., Burger, M., Johnson, R., Coates, A., et al. (2008). Ion and neutral sources and sinks within Saturn's inner magnetosphere: Cassini results. *Planetary and Space Science*, *56*(1), 3–18. https://doi.org/10.1016/j.pss.2007.06.006

Smith, H., Crary, F., Reisenfeld, D., Shappirio, M., Sittler, E., & Woodson, A. (2019). PDS CAPS IMS time-of-flight (TOF) analysis procedures.

Smith, H., Johnson, R., Perry, M., Mitchell, D., McNutt, R., & Young, D. (2010). Enceladus plume variability and the neutral gas densities in Saturn's magnetosphere. *Journal of Geophysical Research*, *115*(A10), A10252. https://doi.org/10.1029/2009ja015184

Smith, H., Johnson, R., Sittler, E., Shappirio, M., Reisenfeld, D., Tucker, O., et al. (2007). Enceladus: The likely dominant nitrogen source in Saturn's magnetosphere. *Icarus*, *188*(2), 356–366. https://doi.org/10.1016/j.icarus.2006.12.007

Smith, H., Shappirio, M., Johnson, R., Reisenfeld, D., Sittler, E., Crary, F., et al. (2008). Enceladus: A potential source of ammonia products and molecular nitrogen for Saturn's magnetosphere. *Journal of Geophysical Research*, *113*(A11), A11206. https://doi.org/10.1029/2008ja013352

Smith, H., Shappirio, M., Sittler, E., Reisenfeld, D., Johnson, R., Baragiola, R., et al. (2005). Discovery of nitrogen in Saturn's inner magnetosphere. *Geophysical Research Letters*, *32*(14), L14S03. https://doi.org/10.1029/2005gl022654

Smith, H. T., Crary, F. J., Dougherty, M. K., Perry, M. E., Roussos, E., Simon, S., & Tokar, R. L. (2018). Enceladus and its influence on Saturn's magnetosphere. In P. M. Schenk, R. N. Clark, C. J. A. Howett, A. J. Verbiscer, & J. H. Waite (Eds.), *Enceladus and the Icy Moons of Saturn* (p. 211). https://doi.org/10.2458/azu_uapress_9780816537075-ch011

Smith, H. T., & Richardson, J. D. (2021). The 3D structure of Saturn magnetospheric neutral tori produced by the Enceladus plumes. *Journal of Geophysical Research: Space Physics*, *126*(3), e2020JA028775. https://doi.org/10.1029/2020ja028775

Spahn, F., Schmidt, J., Albers, N., Hörning, M., Makuch, M., Seiß, M., et al. (2006). Cassini dust measurements at Enceladus and implications for the origin of the E ring. *Science*, *311*(5766), 1416–1418. https://doi.org/10.1126/science.1121375

Spencer, J., Pearl, J., Segura, M., Flasar, F., Mamoutkine, A., Romani, P., et al. (2006). Cassini encounters Enceladus: Background and the discovery of a south polar hot spot. *Science*, *311*(5766), 1401–1405. https://doi.org/10.1126/science.1121661

21699402, 2026, 4, Downloaded from https://agupubs.onlinelibrary.wiley.com/doi/10.1029/2025JA034738 by Los Alamos National Laboratory, Wiley Online Library on [30/07/2026]. See the Terms and Conditions (https://onlinelibrary.wiley.com/terms-and-conditions) on Wiley Online Library for rules of use; OA articles are governed by the applicable Creative Commons License

Teolis, B., & Waite, J. (2016). Dione and Rhea seasonal exospheres revealed by Cassini CAPS and INMS. *Icarus*, *272*, 277–289. https://doi.org/10.1016/j.icarus.2016.02.031

Thomsen, M. F., Reisenfeld, D. B., Delapp, D. M., Tokar, R. L., Young, D. T., Crary, F. J., et al. (2010). Survey of ion plasma parameters in Saturn's magnetosphere. *Journal of Geophysical Research*, *115*(A10), A10220. https://doi.org/10.1029/2010ja015267

Tokar, R., Johnson, R., Hill, T., Pontius, D., Kurth, W., Crary, F., et al. (2006). The interaction of the atmosphere of Enceladus with Saturn's plasma. *Science*, *311*(5766), 1409–1412. https://doi.org/10.1126/science.1121061

Tokar, R., Johnson, R., Thomsen, M., Sittler, E., Coates, A. J., Wilson, R., et al. (2012). Detection of exospheric O2+ at Saturn's moon Dione. *Geophysical Research Letters*, *39*(3). https://doi.org/10.1029/2011gl050452

Tokar, R., Wilson, R., Johnson, R., Henderson, M., Thomsen, M., Cowee, M., et al. (2008). Cassini detection of water-group pick-up ions in the Enceladus torus. *Geophysical Research Letters*, *35*(14). https://doi.org/10.1029/2008gl034749

Tseng, W.-L., Johnson, R., & Elrod, M. (2013). Modeling the seasonal variability of the plasma environment in Saturn's magnetosphere between main rings and Mimas. *Planetary and Space Science*, *77*, 126–135. https://doi.org/10.1016/j.pss.2012.05.001

Vasyliunas, V. M. (1968). A survey of low-energy electrons in the evening sector of the magnetosphere with OGO 1 and OGO 3. *Journal of Geophysical Research*, *73*(9), 2839–2884. https://doi.org/10.1029/ja073i009p02839

Villanueva, G., Hammel, H., Milam, S., Kofman, V., Faggi, S., Glein, C., et al. (2023). JWST molecular mapping and characterization of Enceladus' water plume feeding its torus. *Nature Astronomy*, *7*(9), 1056–1062. https://doi.org/10.1038/s41550-023-02009-6

Wahlund, J., Boström, R., Gustafsson, G., Gurnett, D., Kurth, W., Averkamp, T., et al. (2005). The inner magnetosphere of Saturn: Cassini RPWS cold plasma results from the first encounter. *Geophysical Research Letters*, *32*(20). https://doi.org/10.1029/2005gl022699

Waite, J., & Furman, J. (2022). *Cassini-Huygens Cassini Plasma Spectrometer (CAPS) derived ion moments data collection* (Vol. 29). NASA Planetary Data System.

Waite, J., Jr., Lewis, W., Kasprzak, W., Anicich, V., Block, B., Cravens, T. E., et al. (2004). The Cassini ion and neutral mass spectrometer (INMS) investigation. *Space Science Reviews*, *114*(1), 113–231. https://doi.org/10.1007/s11214-004-1408-2

Waite, J. H., Jr., Combi, M. R., Ip, W.-H., Cravens, T. E., McNutt, R. L., Jr., Kasprzak, W., et al. (2006). Cassini ion and neutral mass spectrometer: Enceladus plume composition and structure. *Science*, *311*(5766), 1419–1422. https://doi.org/10.1126/science.1121290

Waite, J. H., Jr., Lewis, W., Magee, B., Lunine, J., McKinnon, W., Glein, C., et al. (2009). Liquid water on Enceladus from observations of ammonia and 40Ar in the plume. *Nature*, *460*(7254), 487–490. https://doi.org/10.1038/nature08153

Wilson, R., Bagenal, F., Cassidy, T., Fleshman, B., & Crary, F. (2015). The relative proportions of water group ions in Saturn's inner magnetosphere: A preliminary study. *Journal of Geophysical Research: Space Physics*, *120*(8), 6624–6632. https://doi.org/10.1002/2014ja020557

Wilson, R., Bagenal, F., & Persoon, A. (2017). Survey of thermal plasma ions in Saturn's magnetosphere utilizing a forward model. *Journal of Geophysical Research: Space Physics*, *122*(7), 7256–7278. https://doi.org/10.1002/2017ja024117

Wilson, R., Crary, F., Gilbert, L., Reisenfeld, D., Steinberg, J., & Livi, R. (2012). PDS user's guide for Cassini Plasma Spectrometer (CAPS). *Planetary Data System*. https://doi.org/10.17189/1522472

Wilson, R., Reisenfeld, D., Delamere, P., Allen, R., & Cassidy, T. (2021). Revisiting magnetospheric CAPS TOF data post Cassini. *Icarus*, *357*, 114245. https://doi.org/10.1016/j.icarus.2020.114245

Wilson, R., Tokar, R., & Henderson, M. (2009). Thermal ion flow in Saturn's inner magnetosphere measured by the Cassini plasma spectrometer: A signature of the Enceladus torus? *Geophysical Research Letters*, *36*(23). https://doi.org/10.1029/2009gl040225

Wolfe, J., Mihalov, J., Collard, H., McKibbin, D., Frank, L., & Intriligator, D. (1980). Preliminary results on the plasma environment of Saturn from the Pioneer 11 plasma analyzer experiment. *Science*, *207*(4429), 403–407. https://doi.org/10.1126/science.207.4429.403

Wüest, M. (1998). Time-of-flight ion composition measurement technique for space plasmas. *Measurement Techniques in Space Plasmas: Particles*, *102*, 141–155.

Young, D., Berthelier, J., Blanc, M., Burch, J., Coates, A., Goldstein, R., et al. (2004). Cassini plasma spectrometer investigation. *The Cassini-Huygens Mission: Orbiter In Situ Investigations*, *2*, 1–112.

Young, D., Berthelier, J.-J., Blanc, M., Burch, J., Bolton, S., Coates, A., et al. (2005). Composition and dynamics of plasma in Saturn's magnetosphere. *Science*, *307*(5713), 1262–1266. https://doi.org/10.1126/science.1106151

Young, D. T., Waite, J. H., Crary, F. A., & Furman, J. D. (2013). Cassini E/J/S/SW-CAPS-2-UNCALIBRATED-V1.0 [Dataset]. *NASA Planetary Data System*, *16*. https://doi.org/10.17189/1519592

Erratum

The originally published version of this article contained a typographical error in Figures 5 and 6. R_J (Jupiter's radius) has been corrected to R_S (Saturn's radius). This may be considered the authoritative version of record.

21699402, 2026, 4, Downloaded from https://agupubs.onlinelibrary.wiley.com/doi/10.1029/2025JA034738 by Los Alamos National Laboratory, Wiley Online Library on [30/07/2026]. See the Terms and Conditions (https://onlinelibrary.wiley.com/terms-and-conditions) on Wiley Online Library for rules of use; OA articles are governed by the applicable Creative Commons License